ISTITUTO ITALIANO
DI TECNOLOGIA

Università
di Genova

Doctoral School in Neuroscience

Curriculum:

Neuroscience and Neurotechnologies

Cicle XXXVII

Functional Mapping of BLA and CA3 Dendritic Synaptic Inputs in CA1 Pyramidal Neurons of the Ventral Hippocampus

PhD candidate

Vincenzo Regio

Supervisor

Andrea Barberis, PhD

Index

Index 3

Table of Abbreviations 5

Table of Figures 7

Abstract 1

1. Introduction 3

Synaptic connectivity and summation of inputs *3*

Introduction to Synaptic Connectivity 3

Dendritic integration 4

Spatial organization of synaptic inputs 7

Neural Circuits in Emotional Memory Formation: The Role of the Basolateral Amygdala and Ventral Hippocampal CA1 *10*

Valence Encoding in Brain Circuits 10

The Basolateral Amygdala (BLA) 11

The Ventral Hippocampus 16

Neuronal Projections and Valence in BLA-vCA1 Circuits *20*

Experimental Approaches *23*

Galvanometric scanning microscopy 23

Techniques for single-spine calcium imaging 25

Use of optogenetics for interrogating neural circuits 28

Research Objective *30*

2. Methods 31

Animals 31

Surgical procedures 31

Slice preparation 32

Electrophysiological recordings 32

Two-photon images acquisition 33

Automatic ROI drawing and placement 34

Two-photon calcium imaging 36

DeepD3 based semantic segmentation 36

Calcium signals detection 37

Analysis of spine distribution 40

3. Results 41

Automated ROI Placement for High-Precision Spine Calcium Imaging Across Dendritic Trees 41

Combined Optogenetic and Electrical Stimulation to Characterize BLA and SCs Synaptic Inputs 44

Automated Detection and Spatial Analysis of Dendritic Spines in CA1 Pyramidal Neurons 47

Spatial Distribution and Activation Patterns of Calcium Events in Dendritic Spines Following BLA and CA3 Stimulation 50

Branch-Specific Variability Shapes Synaptic Input Distribution 55

4. Discussion 57

Limitations of the study *61*

Future perspectives *62*

Supplementary Figures *63*

Bibliography **64**

Acknowledgments **71**

Table of Abbreviations

AAV	Adeno-Associated Virus
AAV5	Adeno-Associated Virus serotype 5
AM	Acetoxymethyl
AMPA	α-Amino-3-hydroxy-5-methyl-4-isoxazolepropionic Acid
AP	Action Potential / Anterior-Posterior
AT	Array Tomography
BAPTA	1,2-bis(o-aminophenoxy) ethane-N, N', N'-tetraacetic acid
BLA	Basolateral Amygdala
bAPs	Backpropagating Action Potentials
Ca^{2+}	Calcium Ion
CaMKII	Ca/Calmodulin-dependent Kinase Type II
ChR	Channelrhodopsin
ChR2	Channelrhodopsin-2
CNN	Convolutional Neural Network
CNQX	6-Cyano-7-nitroquinoxaline-2,3-dione
CS	Conditioned Stimuli
DG	Dentate Gyrus
EC	Entorhinal Cortex
EPSC	Excitatory Postsynaptic Current
EPSP	Excitatory Postsynaptic Potential
EYFP	Enhanced Yellow Fluorescent Protein
GABA	Gamma-Aminobutyric Acid
GCaMP	Genetically Encoded Calcium Indicator based on Green Fluorescent Protein
GECI	Genetically Encoded Calcium Indicator
GFP	Green Fluorescent Protein
Gsyn	Synaptic Conductance
HSD	Honestly Significant Difference
IQR	Interquartile Range
I/O	Input-Output
LED	Light-Emitting Diode
LTD	Long-Term Depression
LTP	Long-Term Potentiation
Mg^{2+}	Magnesium Ion
mGRASP	Mammalian GFP-Reconstitution Across Synaptic Partners
mPFC	Medial Prefrontal Cortex
Na^{+}	Sodium Ion
NAcc	Nucleus Accumbens
NMDA	N-Methyl-D-Aspartate
NMDAR	N-Methyl-D-Aspartate Receptor
OFC	Orbitofrontal Cortex
pBLA	Posterior Basolateral Amygdala
PFC	Prefrontal Cortex
Ppp1r1b	Protein phosphatase 1 regulatory inhibitor subunit1B

PNs	Pyramidal Neurons
PSF	Point Spread Function
r	Pearson Correlation Coefficient
ReLU	Rectified Linear Unit
RM ANOVA	Repeated Measures Analysis of Variance
ROI	Region of Interest
Rspo2	R-spondin-2 gene
SEM	Standard Error of the Mean
sI/O	Subthreshold Input-Output
SCs	Schaffer Collaterals
SNT	Simple Neurite Tracer
TC	Thalamocortical
vCA1	Ventral Cornu Ammonis Area 1
vHPC	Ventral Hippocampus
VGCC	Voltage-Gated Calcium Channel
VTA	Ventral Tegmental Area
λ	Wavelength
µm	Micrometer
µM	Micromolar

Table of Figures

Figure 1.1. Supralinear vs Sublinear integration 6
Figure 1.2. Amygdala nuclei division 15
Figure 1.3. Dorsal and ventral division of hippocampus 19
Figure 1.4. Projections from the basal nucleus to hippocampus 22
Figure 1.5. Scanning options with Galvanometric system 25
Figure 2.1. Modified Okada filter 38
Figure 2.2. Processing pipeline for denoising 39
Figure 3.1. Automatic ROIs placement on Z-layers 43
Figure 3.2. BLA and SCs stimulation protocol to scan neurons across many z-layers 46
Figure 3.3. Automatic spines detection on the dendritic tree 48
Figure 3.4. Calcium detected signals from BLA and CA3 on dendritic arborization 54
Figure 3.5 Synaptic inputs are unevenly distributed across dendritic branches 56
Figure S1. Event detection control 63

Abstract

Dendritic integration plays a crucial role in neuronal processing, enabling neurons to transform the spatio-temporal patterns of synaptic input activation into action potential output. Pioneering modeling studies and experimental work studies exploiting two-photon glutamate uncaging enabling the stimulation of individual glutamatergic synapses in specific dendritic subdomains demonstrated that specific spatial arrangements of activated dendritic glutamatergic synapses can promote non-linear inputs summation a phenomenon that profoundly affects the probability and the temporal structure of somatic spiking. However, despite the recognized importance of spatial synaptic organization in shaping dendritic integration, our knowledge of how synaptic inputs are arranged across the entire dendritic tree of pyramidal neurons remains limited. Indeed, while anatomical studies utilizing the technique of GFP reconstitution at synapses provide an excellent description of the spatial relationship among synaptic contacts across the whole neuronal dendritic arbor, they fail to identify which inputs are engaged during neuronal activity. On the contrary, functional studies analyzing synaptic activity with calcium or glutamate imaging typically restrict their focus on small dendritic portions. In the present work, we used two-photon laser scanning microscopy to perform calcium imaging at the level of single glutamatergic spines in the whole dendritic tree of pyramidal neurons located in the CA1 region of the ventral hippocampal (vCA1 PNs). In particular, we focused on spines formed by inputs from two specific projections, the basolateral amygdala (BLA) and CA3 (Schaffer Collaterals, SC) that converge onto the vCA1 PNs apical proximal and basal dendrites. By employing a home-written automated region-of-interest detection algorithm we analyzed approximately 1,300 spines per neuron and examined synaptic activation patterns induced by optogenetic and electrical stimulation of BLA and SC inputs, respectively. Our results reveal that BLA inputs are more evenly distributed between apical and basal dendrites, whereas CA3 inputs predominantly target apical compartments. Interestingly, spine density varies across dendritic branches, with third-degree apical dendrites exhibiting the highest density of both total and activated spines.

These findings highlight distinct spatial synaptic organization patterns for BLA and CA3 inputs, suggesting that specific dendritic branches may have specialized roles in integrating input-specific signals.

1. Introduction

Synaptic connectivity and summation of inputs

Introduction to Synaptic Connectivity

Neurons communicate by transmitting signals via their axon and by receiving synaptic inputs from other neurons onto dendrites. Activation of synaptic inputs generates a post-synaptic potential in dendrites that propagates bidirectionally: centripetally toward the soma and axon hillock, where signals are integrated to potentially generate a somatic action potential (AP), and centrifugally along the dendritic tree. Depending on neurotransmitters released presynaptically and the receptors expressed on the postsynaptic neuron, a synapse can be excitatory or inhibitory. Excitatory synapses (releasing glutamate or acetylcholine) typically induce a depolarization across the postsynaptic membrane, whereas inhibitory synapses (releasing glycine or gamma-aminobutyric acid, GABA) generally induce shunting and hyperpolarization in mature neurons. Individual neurons continuously process thousands of synaptic inputs and operate an input-output (I/O) transformation to produce a pattern of action potentials (APs).

Different theoretical approaches have been developed to describe the integration of excitatory and inhibitory synaptic signals. According to the simplest model, neuronal cells are conceptualized as “point neurons" (McCulloch and Pitts, 1943) in which synaptic inputs are linearly summed, and an action potential (AP) is generated when the overall depolarization crosses the AP voltage threshold. In this theory, where every synaptic input in the neuron equally contributes to the overall response (*i.e.* neuronal output), the neuron is reduced to a thresholding device unable to perform complex operations. However, several lines of evidence suggest that dendritic dynamics can significantly extend neuronal processing power. Dendrites are considered semi-independent thresholding units of input processing, capable of generating a rich input/output transformation due to nonlinear input summation. For instance, neurons can use dendrites to perform complex tasks such as

coincidence detection, information selection, routing, and multiplexing, low-pass filtering, parallel processing and can solve complex logics problems such as Boolean linearly non-separable functions (Poirazi, Brannon and Mel, 2003; Naud and Sprekeler, 2018; Pagkalos, Chavlis and Poirazi, 2023).

Dendritic integration

Dendritic integration refers to the process by which incoming synaptic signals are processed within the dendrites, where they are combined to influence the generation of action potentials at the somatic level. As mentioned above, dendrites support non-linear input summation, meaning that the observed depolarization resulting from the simultaneous activation of multiple inputs may not equals that the expected depolarization calculated as the arithmetic sum of the depolarizations generated by each individual input. Plotting observed vs expected depolarization reveals three distinct types of operations that dendrites can perform: linear (observed equals expected), supralinear (observed exceeds expected), and sublinear (observed is lower than expected) integration. Neurons perform non-linear operations based on the passive and active properties of their dendrites. Passive properties, such as synaptic conductance (Gsyn), ionic driving force, membrane resistance, capacitance, and space constant determine the amplitude and time course of synaptic inputs. For instance, in the case that multiple synaptic inputs activate, the local driving force can locally decrease thus leading to sublinear input summation (Martin, 1955). In contrast, active dendritic conductances, including those mediated by N-methyl-D-aspartate receptors (NMDA receptors or NMDARs), sodium (Na+), calcium (Ca2+), and potassium (K+) channels, have been shown to play a crucial role in shaping the subthreshold input-output (sI/O) relationships in neurons. The activation of such receptors and voltage-dependent channels is influenced by several factors including the passive properties of the dendrites, the voltage-dependence of channel gating, and their spatial distribution along the dendrite. Depending on whether these channels mediate inward (depolarizing) or outward (hyperpolarizing) currents, they can either enhance or dampen local depolarizations,

respectively. This process can result in sublinear, linear, or supralinear dendritic operations (Figure1; Branco and Häusser, 2011; Chiovini *et al.*, 2014). When depolarizing conductances are engaged with proper temporal synchrony and within a dendritic segment, they produce all-or-none regenerative responses known as dendritic spikes (Losonczy and Magee, 2006). Sodium spikes triggered by high-amplitude local depolarization are brief and are likely associated with the entry of calcium. They propagate throughout the dendritic tree toward the soma where they can trigger somatic spikes. Ca^{2+} and NMDA spikes are longer, plateau-like events that require the synchronous activation of many synapses and are often localized to specific regions of the dendritic tree (Larkum, 2013). In pyramidal neurons, calcium spikes can propagate to the soma whereas NMDA spikes are usually restricted to local dendritic compartments. In cortical layer 5 pyramidal neurons, NMDA spikes in the distal tuft can facilitate Ca2+ spikes, enabling distal synaptic inputs to contribute to neuronal firing (Larkum *et al.*, 2009). In this way, few inputs temporally and spatially constricted produce regenerative events amplifying the depolarization and increasing the likelihood for the neurons of reaching the spike threshold. Moreover, it should be noted that ionic conductances can also support the backpropagation of somatic APs to the dendrites (Stuart *et al.*, 1997). The presence of bAPs coupled with synaptic activity could create the conditions for the neuron to initiate burst activity (Larkum, Zhu and Sakmann, 1999).

Another important determinant that plays an important role in the integration of inputs is dendritic morphology. Large caliber dendrites, which have a large space constant, experience minimal loss of driving force and tend to summate few inputs linearly. However, due to expression of the aforementioned voltage-gated channels the simultaneous or short timed input activation of many synaptic inputs can also lead to supralinear summation and can initiate regenerative events. In contrast, thin dendrites typically exhibit sublinear integration (Abrahamsson *et al.*, 2012) but, compared to thick dendrites, can more easily engage regenerative events through the activation of NMDARs and Ca^{2+} channels.

This intricate balance between dendritic morphology, the expression of voltage-gated channels, and timing of synaptic input creates a complex system for neuronal computations. However, understanding how these mechanisms shape integration is further

enriched by insights from computational models and in vitro experiments, which highlight the interplay between excitatory and inhibitory inputs at the dendritic level as another key factor contributing to the computational framework. Both *in silico* and *in vitro* studies showed that inhibitory synapses might have a prominent role in regulating dendritic integration in more distal synapses and in a location-dependent manner (Jadi *et al.*, 2012; Lovett-Barron *et al.*, 2012; Palmer, Murayama and Larkum, 2012). For example, even small inhibitory conductances localized on the same dendritic segment can dampen NMDAR-assisted supralinear integration (Rhodes, 2006).

In summary, the interplay between active, passive and morphological properties determines the input/output relationship.

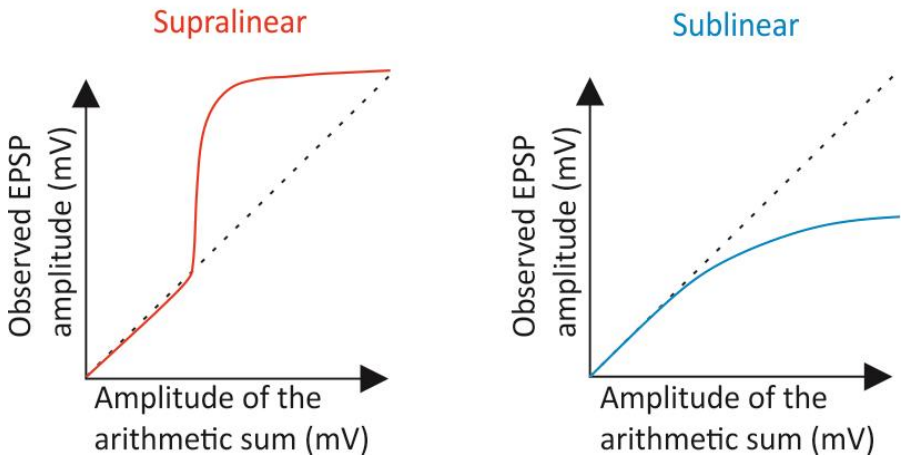

Figure 1.1. Supralinear vs Sublinear integration
Under a certain threshold, inputs are summed linearly (dotted line). Over the threshold, based on the characteristics of the cell and its dendrites, inputs are summed supralinearly (over the expected arithmetic sum) or sublinearly (below the arithmetic sum).

Spatial organization of synaptic inputs

By using computational models, Poirazi and Mel (Poirazi and Mel, 2001) provided crucial insights into how neurons use dendritic compartmentalization for enhanced computational and storage capacity. Furthermore, they suggested that clustered synaptic inputs along dendrites promote dendritic spike initiation (Poirazi, Brannon and Mel, 2003). In support of the importance of spatial arrangements in dendritic integration and dynamics, Polsky *et al*. (Polsky, Mel and Schiller, 2004) demonstrated experimentally that activating glutamatergic inputs within ~40 µm results in supra-linear summation, indicating that a clustered synaptic organization may favor the initiation of dendritic spikes. Moreover, imaging studies of glutamatergic inputs activity in dendrites further analyzed and demonstrated the presence of functional synaptic clusters. In fact, spontaneous activity in pyramidal neurons both in CA3 and L2/3 tends to activate glutamatergic spines that are positioned contiguously within the same dendritic segment, thus forming small clusters within ~10 µm defined "synaptic assemblets" (Takahashi *et al.*, 2012). Together with this, it has been shown that in developing hippocampal neurons, synaptic inputs tend to cluster together based on their correlated activity (Kleindienst *et al.*, 2011). These functional data have been corroborated by anatomical studies analyzing the structural synaptic mapping demonstrating that, in neocortical and hippocampal pyramidal neurons, the spatial organization of synaptic inputs formed by specific fibers onto the dendritic tree of pyramidal neurons appears to be highly structured (Rah *et al.*, 2013; Druckmann *et al.*, 2014).

Plasticity mechanisms are also shown to be involved in maintenance and formation of dendritic clusters.

For instance, the stimulation of an individual glutamatergic spine not only induces long-term potentiation (LTP) at the stimulated spine but also lowers the threshold for inducing LTP at neighboring spines within the range of 10 µm, a phenomenon referred to as coordinated plasticity or heterosynaptic plasticity (Harvey and Svoboda, 2007). Notably, the larger dimensions of clustered spines suggest that these synapses are more likely to undergo potentiation, reflecting their enhanced strength and stability (Takahashi *et al.*, 2012). By forming functionally relevant activity ensembles (or hot spots), synapse clustering plays a

crucial role in supporting learning and memory. For example, Frank et al. (Frank *et al.*, 2018) examined the relationship between synaptic turnover and memory performance using *in vivo* 2-photon microscopy. They found that increased spine turnover before the learning phase was correlated with improved post-learning task performance and with a higher probability of synapse clustering. They also found that in mice models with enhanced spine turnover, there was an associated increase in both memory performance and synapse clustering. These results suggest that localized synaptic turnover, particularly in dendritic hotspots, could serve as a substrate for memory-enhancing synapse clustering. Similarly, long-term depression (LTD) at single spine can either potentiate or depress neighboring spines (Chater and Goda, 2021). Overall, these findings suggest that short-range plasticity interactions between spines contribute shaping the spatial organization of dendritic glutamatergic synapses. Anatomical and detailed circuit mapping at the micro-scale corroborates the predictions by Poirazi and Mel (2001). Using array tomography (AT) to image thalamocortical (TC) input onto L5 pyramidal neurons at the nanometer scale, it has been (Rah *et al.*, 2013) observed that TC inputs colocalize in dendritic portions, forming synaptic clusters supporting non-linear dendritic integration and promoted clustered plasticity. Similarly, Druckmann and colleagues (Druckmann *et al.*, 2014)employed the mammalian GFP-Reconstitution Across Synaptic Partners (mGRASP) technique to investigate CA3 Schaffer collateral inputs on CA1 pyramidal neurons. Interestingly, they showed that many branches were either more or less innervated than expected by chance, highlighting branch-level variability in synaptic connectivity for both basal and apical dendrites. In particular, non-random distributions were observed when branches were organized according to their position within the electrical signal pathway. This means they analyzed branches in relation to how signals travel from the most distal terminal branches toward the soma. By grouping branches along this pathway, it became evident that synaptic connectivity was not uniformly distributed. Instead, specific branches, depending on their location within this pathway, exhibited distinct patterns of innervation, suggesting a functional organization tied to the directional flow of electrical signals within the neuron. This structured connectivity adds to

growing evidence that synaptic clustering is a common structural motif in the brain, enabling neural circuits to process information more effectively.

However, not all the studies carried out in dendrites of PNs univocally reported a clearly clustered synaptic organization. Three different *in vivo* studies in three different brain areas (visual cortex, barrel cortex, and auditory cortex) showed that stimuli carrying similar information were not clustered on dendrites but were rather distributed in a "salt and pepper" fashion (Jia *et al.*, 2010; Chen *et al.*, 2011; Varga *et al.*, 2011), a result that seems to conflict with the "input clustering theory". However, later studies confirmed that synaptic inputs carrying similar information do cluster in specific dendritic subdomains. At the level of the visual cortex, neurons tuned to specific orientations contact the same sub-regions on apical and basal dendrites of L2/3 PNs, a spatial arrangement that contribute to the improved detection of edge detection and visual contour integration (Iacaruso, Gasler and Hofer, 2017). Similarly, in the motor cortex, synaptic inputs from neurons encoding specific sensorimotor tasks are clustered in PNs dendrites. Overall, these data indicate that, while input clustering is not an obligatory configuration, it remains a fundamental property of dendritic organization.

According to Kastellakis et al. (Kastellakis *et al.*, 2015), functional clusters do not simply encode basic sensory features. Instead, they are thought to combine multiple features to represent meaningful natural stimuli. From this perspective, a cluster does not merely represent an ordered sequence of simple sensory inputs, such as different sound frequencies (Hz). Rather, it integrates these inputs into a cohesive representation of complex, conceptually relevant stimuli. For example, in the auditory cortex, a cluster might consist of synapses specifically tuned to the range of frequencies that make up natural speech, capturing the essence of the stimulus rather than its individual components.

Neural Circuits in Emotional Memory Formation: The Role of the Basolateral Amygdala and Ventral Hippocampal CA1

Valence Encoding in Brain Circuits

Valence refers to the emotional component of an event, an object or a situation. In the context of memory, valence determines the emotional significance of an experience, influencing whether it is encoded as a positive or negative memory. Positive valence is typically associated with rewarding or pleasurable experiences, while negative valence is linked to aversive or unpleasant experiences (Frijda, 2017). The emotional attribute of a memory is significantly relevant in shaping future behaviors by promoting approach and avoidance (Lang, 1995). The idea of valence as an emotional component existed before the neuroscientific understanding of the computational mechanisms involved in valence processing. During the recent decades, research in the neuroscience field has started to identify brain hubs essential for valence processing. Although emotional encoding is a process carried out by many brains areas, some regions are particularly important in categorizing emotion along the dimensions of valence (whether the stimulus is positive or negative) and salience (how significant is the stimulus) (Xiu *et al.*, 2014). Many studies have examined valence assignment in relation to specific brain regions. For example, as part of the mesolimbic pathway, which includes dopaminergic projections from the ventral tegmental area (VTA), the NAcc is central to processing both reward and aversive signals (Schultz, 2000; Carlezon and Thomas, 2009; Russo and Nestler, 2013; Namburi *et al.*, 2015). VTA-NAcc projections send both reward and aversive stimuli making the NAcc one of the core regions responsible for decoding rewarding and aversive signals from the VTA (Carlezon and Thomas, 2009; Soares-Cunha *et al.*, 2020).

In parallel, the medial prefrontal cortex (mPFC) plays a key role in the integration and evaluation of valence to guide future behavioral responses. It tightly interplays with other subcortical structures such the NAcc in the top-down control of emotional responses (Etkin, Egner and Kalisch, 2011).

The mPFC is activated by both positive and negative stimuli, supporting its role in encoding the valence of experiences (Roy, Shohamy and Wager, 2012). Additionally, it interacts with the orbitofrontal cortex (OFC), a region crucial for assessing the emotional significance of stimuli and adapting behavior to changing contexts (Rolls, 2004). By combining sensory input with internal states and past experiences, the PFC (including the OFC) influences decision-making processes, emphasizing its role in assigning valence.

In addition to the NAcc and mPFC, the amygdala is a crucial brain region for valence encoding. It is particularly reactive to emotionally significant cues, facilitating the rapid identification of both threats and positive outcomes (LeDoux, 2000). The amygdala's extensive connections with the mPFC and other cortical areas allow it to integrate emotional and cognitive information, generating appropriate behavioral responses (Pessoa, 2008). Due to its high connectivity within and beyond the amygdala nuclei, the amygdala is often regarded as a critical anatomical and functional crossroad in the processing of valence and emotion (Swanson and Petrovich, 1998; LeDoux, 2000; Paton *et al.*, 2006; Tye *et al.*, 2008; Shabel and Janak, 2009). Moreover, the ventral region of the hippocampus (vHPC) supports valence-related activity through its direct connections with other brain regions involved in valence processing. vHPC, indeed, shows an extensive connection pathway with all the three aforementioned brain regions modulating place preference in rewarding situations or anxiety-like behaviors, depressive-like behaviors, and fear extinction.

The Basolateral Amygdala (BLA)

The amygdala is a cerebral structure evolutionary conserved across vertebrates and formed by a heterogeneous complex of multiple subnuclei and neuronal cell types. Its role has been linked with emotions processing, social behavior, decision-making, and both instinctive and motivated behaviors (LeDoux, 2000). It is located deep in the temporal lobe in humans and non-human primates while in rodents it is found in the caudoventral forebrain (Swanson and Petrovich, 1998). Among species, although many similarities are reported, there are clear differences in connectivity, relative size, and interconnectivity in the nuclei of the amygdala (Swanson & Petrovich, 1998). In this introduction to the various nuclei of the amygdala, we

will use the nomenclature developed by Prince et al. (Price *et al.*, 1987) specifically for describing this brain structure in rodents. In this classification, the amygdala can be divided into three major groups of nuclei: basolateral nuclei (BLA), cortical-like nuclei, and centromedial nuclei (Fig. 2, from Sah *et al.*, 2003). The amygdala receives sensory information from all modalities. Data from studies based mostly on anterograde or retrograde tracers show that the amygdaloid complex is targeted at all levels (A Pitkänen *et al.*, 2000). Moreover, these inputs can arise from both primary cortex and associative areas. Olfactory, somatosensory, gustatory, and visceral inputs arise mostly from primary sensory cortices, while auditory and visual information arrive to the amygdala from associative areas (Swanson and Petrovich, 1998). Importantly, not only sensory stimuli innervate the amygdala but also several sources of polymodal information such as the hippocampus, prefrontal cortex, and perirhinal cortex (A Pitkänen *et al.*, 2000).

Efferent connections of the amygdala nuclei are widespread and mostly direct to cortical and subcortical targets. Among subcortical targets, we find the hypothalamus and brain stem areas that are reached by amygdala projections originating in the centromedial nuclei. Although the central amygdala projects mainly to subcortical structures, the basolateral nuclei have less specification. In fact, they project to both cortical (such as the prefrontal cortex and perirhinal cortex) and subcortical structures (such as the hippocampus, nucleus accumbens, and thalamus) (Swanson and Petrovich, 1998).

Moreover, interconnections between amygdala nuclei are abundant and crucial for emotional memories formation and sensory encoding. BLA and cortical-like nuclei show reciprocal connectivity facilitating emotional processing (Pitkänen, Savander and LeDoux, 1997; Swanson and Petrovich, 1998). Moreover, BLA sends information to the central nucleus which coordinates autonomic and behavioral response thanks to its projection to hypothalamus and brainstem (Moga *et al.*, 1990; Rizvi *et al.*, 1991).

The basolateral nucleus specifically combines sensory information with emotional valence to modulate behaviors and memories. Since it receives diverse sensory inputs from the thalamus and from cortical areas, BLA can process a wide range of sensory stimuli assessing their emotional weight. The ability to integrate different inputs makes BLA essential for the

formation of associative memories. Behavioral studies in rats and mice have shown that amygdala is essential for fear conditioning, a well-established model of emotional memory. The acquisition and the retrieval of the fear memory is abolished by bilateral BLA lesion, indicating its key role in these specific mnemonic processes (Fanselow and LeDoux, 1999). Electrophysiological investigation confirmed the role of BLA in formation of emotional memories showing that long-term potentiation (LTP) occurs within the BLA during fear conditioning (Rogan, Staubli and LeDoux, 1997). Moreover, encoding and strengthening of emotional experiences is orchestrated by amygdala thanks to reciprocal connections with the hippocampus and the prefrontal cortex. BLA fibers projecting to PFC shape how emotional experiences guide future behaviors (Burgos-Robles *et al.*, 2017; Huang *et al.*, 2020), while BLA projections to vHPC integrate emotional significance with contextual details of an experience (Pitkänen *et al.*, 2000). Contrary to the traditional role that classifies the BLA as a stress-related and negative emotions detector, it has been shown to contribute to reward-related learning and positive valence detection. BLA neurons show excitatory responses to conditioned stimuli (CS) paired with rewarding or aversive outcomes (Schoenbaum, Chiba and Gallagher, 1998; Zhang and Li, 2018). Although still debated, it seems that BLA is required for the acquisition of stimulus-reward association, but it is not required for its expression. Acquisition of rewarding Pavlovian association relies on BLA-NAcc projections since optogenetic inactivation of BLA-NAcc projecting fibers impairs licking behavior for sucrose in response to a predictive cue (Ambroggi *et al.*, 2008). Moreover, extensive literature shows that BLA-NAcc projections are also implicated in the acquisition and expression of conditioned place preference for a food reward (Everitt *et al.*, 1991; White and McDonald, 1993; Schroeder and Packard, 2002).

BLA has a functional diversity along the anterior-posterior axis. Anterior BLA (aBLA) seems to make a great contribution in fear conditioning experiments (Goosens and Maren, 2001), while posterior BLA (pBLA) seems to be mainly involved in reward conditioning (Kantak *et al.*, 2002). Moreover, intriguing findings from the Tonegawa's group showed that two genetically different BLA populations could drive a behavioral response consistent with the valence of the experience (Kim *et al.*, 2017). These two segregated groups of neurons seem to

correspond to the previously described magnocellular and parvocellular amygdaloid neuron (Alheid, 2003). Neurons in the anterior BLA are positive for the R-spondin-2 (Rspo2) gene and correspond to the magnocellular neurons, while cells in the posterior parts express the gene Ppp1r1b, coding for protein phosphatase 1 regulatory inhibitor subunit1B and correspond to the parvocellular neurons (Kim *et al.*, 2017). In conclusion, the mechanisms involving synaptic plasticity, hormonal modulation, and intricate neural connectivity highlight the importance of the BLA in both the acquisition and the consolidation of emotional memories, influencing behaviors and decision-making processes based on past emotional experiences.

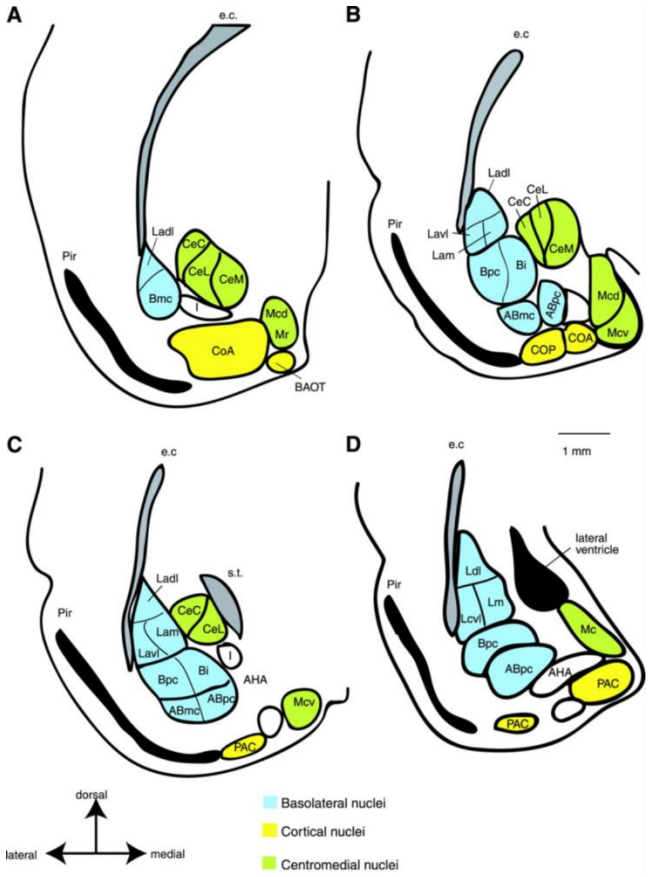

Figure 1.2. Amygdala nuclei division

Coronal sections are shown from rostral (A) to caudal (D). The nuclei are organized into three divisions: basolateral (blue), cortical (yellow), and centromedial (green). Key structures, including the external capsule (e.c.), piriform cortex (Pir), and stria terminalis (s.t.), are labeled for orientation.

A.Rostral Section.

Basolateral nuclei (blue): Ladl (Lateral, dorsal), Bmc (Basomedial, central), CeC (Central, central), CeL (Central, lateral), CeM (Central, medial)

Cortical nuclei (yellow): CoA (Cortical, anterior). Centromedial nuclei (green): Mcd (Medial, dorsal), Mr (Medial, rostral).

B. Intermediate-Rostral Section.

Basolateral nuclei (blue): Ladl (Lateral, dorsal), Lam (Lateral, medial), Lavl (Lateral, ventrolateral), Bpc (Basolateral**,** posterior, central), Bi (Basolateral, intermediate), ABmc (Accessory basal, magnocellular). Cortical nuclei (yellow): CoA (Cortical, anterior), COP (Cortical, posterior)

Centromedial nuclei (green): Mcd (Medial, dorsal), Mcv (Medial, ventral)

C. Intermediate-Caudal Section

Basolateral nuclei (blue): Ladl (Lateral, dorsal), CeC (Central, central), CeL (Central, lateral), Lam (Lateral, medial), Lavl (Lateral, ventrolateral), Bpc (Basolateral, posterior, central), Bi (Basolateral, intermediate), ABpc (Accessory basal, parvocellular) Cortical nuclei (yellow): PAC (Periamygdaloid cortex) Centromedial nuclei (green): Mcv (Medial, ventral)

D. Caudal Section

Basolateral nuclei (blue): Ld (Lateral, dorsal), Lm (Lateral, medial), Lcvl (Lateral, central, ventrolateral), Bpc (Basolateral, posterior, central), ABpc (Accessory basal, parvocellular) Cortical nuclei (yellow): PAC (Periamygdaloid cortex) Centromedial nuclei (green): Mc (Medial, central). Form Sah et al., 2003

The Ventral Hippocampus

The hippocampal formation, a small seahorse-shaped structure in the temporal lobe, is a well-conserved region found in all mammals, including rodents (Sauvage, Nakamura and Beer, 2013). It consists of dentate gyrus (DG), the subiculum, the entorhinal cortex (EC), and the hippocampus proper. The hippocampus proper, in turn, is composed of the cornu ammonis (CA), which is further divided into three fields: CA1, CA2, and CA3 (Schultz and Engelhardt, 2014). The Hippocampus plays a central role in memory formation, spatial navigation, and emotion regulation.

The hippocampal formation exhibits extensive connectivity with other brain regions and intricate intra-hippocampal connections. Neurons in Layer II of EC neurons provide direct inputs both to granule cell of the dentate gyrus and CA3 pyramidal neurons (perforant path), while neurons in layer III of EC project directly to CA1. The perforant path then connects the DG to CA3 and CA3 to CA1, forming the well-known trisynaptic loop (Andersen, Bliss and Skrede, 1971). Fibers from granule cells of the DG that connect to CA3 are known as *Mossy Fibers,* while axons from CA3 pyramidal cells projecting to CA1 are called Schaffer collaterals (SCs). CA1 projects to subiculum and layer III of the EC closing the loop. To understand the complexity of the trisynaptic loop, it is essential to note that the Cornu Ammonis is organized into distinct layers (strata). From the deepest to the most superficial, these includes the stratum oriens, which contains the cell bodies of the inhibitory basket cells and the basal dendrites of the pyramidal cells; the stratum piramidale, which houses the cell bodies of the pyramidal neurons and inhibitory bistratified cells; the stratum radiatum, which contains Schaffer collaterals fibers from CA3 to CA1; and the Stratum lacunoso-molecolare, the most superficial layer, which contains fibers from both Schaffer collateral and the perforant path that synapse on the apical tuft of CA1 pyramidal neurons.

The hippocampus can be anatomically and functionally divided into the dorsal (in rodents, posterior in humans) and ventral (in rodents, anterior in humans) section (Fig. 3).

The dorsal hippocampus is primarily involved in spatial learning and memory, playing a crucial role in the formation of spatial maps and navigation (Moser, Moser and Andersen, 1993; Bannerman *et al.*, 2004). Lesions of this region impair performance in spatial memory

tasks, such as the Morris water maze (Moser *et al.*, 1995). In contrast, the ventral hippocampus is more associated with emotional processing and anxiety (Fanselow and Dong, 2010). Damage of this area reduced the anxiety-related behaviors, as evidenced by lesioned mice showing less anxiety in elevated plus maze tests and reduced fear in the conditioning experiments (Kjelstrup *et al.*, 2002). Furthermore, gene expression gradients along the dorsoventral axis of the CA1 subregion suggest functional differences between these two hippocampal areas (Cembrowski *et al.*, 2016).

The ventral CA1 (vCA1) region has strong connections with cortical and subcortical areas involved in social approach behaviors, anxiety-like behaviors, reward, and stress response. These include the mPFC (Jay and Witter, 1991), the NAcc (Okuyama *et al.*, 2016), the lateral hypothalamus (LH) (Herman and Cullinan, 1997), and the basal and central amygdala (A Pitkänen *et al.*, 2000). Subpopulations of vCA1 neurons exhibit strong electrophysiological responses and encode spatial stimuli in anxiogenic areas of the elevated plus maze (EPM) (Ciocchi *et al.*, 2015; Jimenez *et al.*, 2018). Specifically, neurons projecting to the lateral hypothalamus (LH) or medial prefrontal cortex (mPFC) modulate exploration by increasing their firing rates in response to these areas. It has been proposed that vCA1-LH drives a rapid avoidance response, while vCA1-mPFC may serve as a slower, higher-order pathway for avoidance behaviors, projecting to the amygdala, hypothalamus, or periaqueductal gray (Jimenez *et al.*, 2020). Unlike the projections to the mPFC and LH, vCA1 neurons projecting to the basal amygdala (BA) do not appear to encode innate anxiogenic features in anxiety-based assays. Instead, they respond to foot shocks in contextual fear conditioning and are essential for encoding context-fear associations (Jimenez *et al.*, 2018; Graham *et al.*, 2021). Thus, vCA1 may influence anxiety behaviors by directly encoding threatening stimuli through specialized anxiety cells that represent innately anxiogenic environments. These anxiogenic signals may originate from within the hippocampal circuit itself (e.g., CA3) or from external sources such as the BLA, which has direct connections to vCA1 and is linked to anxiety-related behaviors (Felix-Ortiz *et al.*, 2013; Felix-Ortiz and Tye, 2014). However, it is unlikely that the amygdala activates anxiety-related cells in CA1, as single-unit recordings indicate that BLA neurons are more active in the secure, closed arm of the EPM, in contrast to the

activity pattern of vCA1 anxiety cells (Adhikari *et al.*, 2015). Additionally, BLA neurons projecting to vCA1 respond to cues of both positive and negative valence (Beyeler *et al.*, 2016), whereas vCA1 anxiety cells are more specifically tuned to anxiety stimuli (Jimenez *et al.*, 2018). For these reasons, a more likely external source of anxiogenic input could be the entorhinal cortex (EC), which processes environmental cues associated with anxiety-provoking contexts (Diehl *et al.*, 2017). The EC, which plays a key role in integrating sensory and contextual information, may send signals to the vCA1 that contribute to the encoding of threatening stimuli. This could help explain how vCA1 participates in the modulation of anxiety behaviors by responding to contextually relevant cues that signal potential threats.

A recent study has also highlighted the role of the ventral hippocampus in reward processing. Specifically, the projection from vCA1 to NAcc is involved in both place-preference induced by reward (Sosa, Joo and Frank, 2020) and the hedonic aspects of food, regulating meal approach and consumption independently of location (Reed *et al.*, 2018; Wee *et al.*, 2021).

Thus, different brain regions receive input from the ventral hippocampus, with divergent outputs encoding different types of stimuli and contributing to various behaviors. Despite its predominant anxiogenic role, ventral hippocampus is involved in different valence processing, such as reward and fearful stimuli. Notably, vCA1 projections are largely segregated, with only a small portion of neurons projecting to multiple targets. However, recent evidence suggests that neurons with different downstream targets may share similar presynaptic inputs, supporting the idea that the vCA1 region functions as a central hub, integrating diverse information and transmitting it to multiple downstream areas (Gergues *et al.*, 2020).

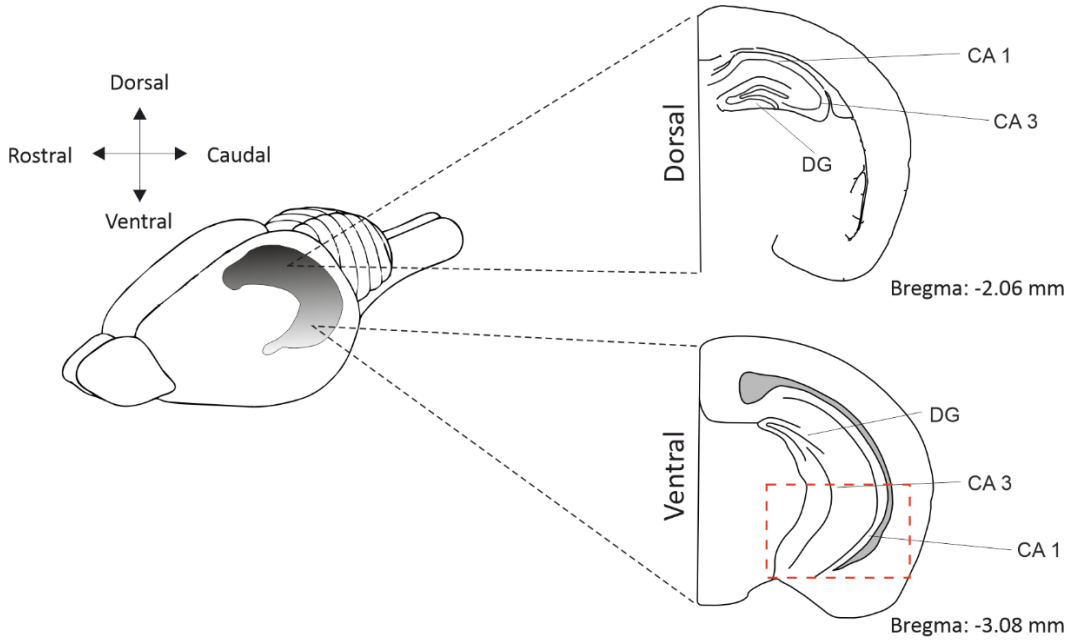

Figure 1.3. Dorsal and ventral division of hippocampus
Left panel shows a schematic of the rodent brain with the hippocampus highlighted. The right panels display coronal sections of the hippocampus at two different rostrocaudal positions relative to bregma. The upper section (Bregma -2.06 mm) shows the dorsal hippocampus, including CA1, CA3, and the dentate gyrus (DG). The lower section (Bregma -3.08 mm) shows the ventral hippocampus, outlined by the dotted box, with regions CA1, CA3, and DG labeled.

Neuronal Projections and Valence in BLA-vCA1 Circuits

The BLA provides dense innervation to the vHPC (Fig. 4, Pikkarainen *et al.*, 1999), establishing a circuit essential for integrating emotional and spatial information. This connection plays a pivotal role in anxiety-related behaviors, as both regions are extensively studied for their involvement in processing fear, stress, and avoidance responses (Davidson, 2002; Kjelstrup *et al.*, 2002; Bannerman *et al.*, 2003; Kheirbek *et al.*, 2013). Tye's group investigated the role of the BLA projection to the vHPC (Felix-Ortiz *et al.*, 2013) in different behavioral tasks. First, they highlighted that optogenetic activation of BLA projection to vHPC positively modulates anxiety-related behaviors. Second, since vHPC has been showed to be involved in social interaction in rodents (Cadogan *et al.*, 1994), they also investigated the role of the aforementioned projections in mice social behavior, showing that optogenetic inhibition of BLA terminals in vHPC leads to increased pro-social behavior in a resident-intruder paradigm (Felix-Ortiz and Tye, 2014). These works allowed establishing a functional bidirectional role for BLA-vHPC projections.

Since most BLA neurons exhibit low, stable firing rates, the small variations in the activity of these neurons may still carry important information. Notably, amygdala neurons that respond to emotional valence can be either excited or inhibited depending on whether the stimulus is perceived as positive or negative. Thus, even a slight change in the firing patterns of these neurons could encode the valence (emotional value) of a given stimulus (Beyeler *et al.*, 2016). Further investigations by Tye's group revealed that positive and negative associative memories are encoded by anatomically distinct circuits within the BLA based on the valence of the memory. They found that approximately half of the BLA neurons responded to both positive and negative valence cues, indicating their ability to process a wide range of emotional information. Notably, these BLA-vHPC projectors did not show a preference for encoding either positive or negative emotional memories. Additionally, the distribution of BLA neurons has been shown to be sparse and intermixed across different regions, with vHPC projectors being denser in the posterior-ventral BLA but evenly distributed along the lateral, medial, and dorsal axes (Beyeler *et al.*, 2018). This contrasts with earlier studies that identified two genetically defined populations along the anterior-

posterior axis of the BLA (Kim *et al.*, 2016), suggesting different organizational structures for processing emotional valence.

However, further investigations were performed to assess whether the BLA–vCA1 inputs are structurally and functionally uniform along the anterior–posterior axis of the BLA and the superficial-deep axis of vCA1. Guilin Pi and colleagues in 2020 underlined that neurons in the aBLA and pBLA innervate the deep layer Calbidin 1 negative (Calb1−) neurons and the superficial layer Calb1+ neurons of vCA1, respectively. Moreover, by using optogenetic, they dissect the function of these projections showing that the aBLA–vCA1 inputs were anxiogenic, while pBLA–vCA1 inputs were anxiolytic (Pi *et al.*, 2020). So, they proposed that aBLA and pBLA send parallel and non-overlapping inputs to vCA1 and that differential information flows through these two distinct circuits.

Interestingly, amygdala sends both excitatory and inhibitory signals to both glutamatergic and GABAergic neurons of the vCA1 (Alsubaie *et al.*, 2021). Moreover, the balance of these excitatory and inhibitory inputs determines the activity of the downstream target of the aforementioned neurons. In fact, when only the excitatory signals from the BLA are engaged, they primarily stimulate the pyramidal cells in the vCA1 that send information back to the amygdala. On the other hand, when both excitatory and inhibitory signals are present, they strongly activate a second population of pyramidal neurons that project to the NAcc. This activation promotes place preference and motivated behaviors.

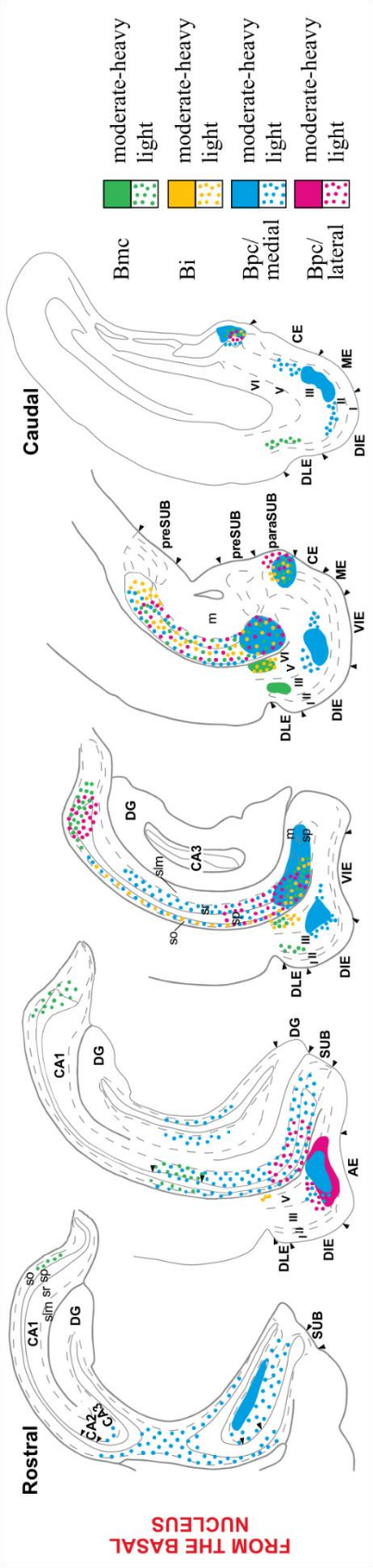

Figure 1.4. Projections from the basal nucleus to hippocampus

The color code in the box on the right side of each panel indicates the origin and density of projections. In panels (A–C), coronal sections progress from rostral to caudal. Arrowheads mark the anatomical boundaries of different regions within the hippocampal formation. In the entorhinal cortex, dashed lines distinguish the layers, labeled with Roman numerals (I–VI). The rostrocaudal position relative to bregma is noted below each section. (Paxinos and Watson, 1986). From Pikkarainen et al., 1999

Experimental Approaches

Galvanometric scanning microscopy

Conventional light microscopy works by illuminating the entire sample and capturing light from the entire field of view simultaneously. Light passing through the sample (in transmitted light microscopy) or emitted from the sample (in epifluorescence microscopy) is captured directly by a camera or eyepiece to form an image. The resolution, typically around 200 nm, is limited by the diffraction of visible light, which is inherently tied to the wavelength of the light used and the numerical aperture (NA) of the objective lens. According to the Abbe diffraction limit, resolution improves with shorter wavelengths of light and higher NA. In scanning microscopy, the sample surface is imaged point-by-point using a focused laser beam. One of the most widely used methods for live imaging is confocal laser scanning microscopy, where a laser beam scans the sample point by point, and the emitted fluorescence light is collected through a pinhole to achieve optical sectioning and high-resolution imaging. While this technique prevents out-of-focus light, the acquisition speed is typically slow. Spinning disk confocal microscopy overcomes this limitation by using multiple pinholes arranged in an Archimedean spiral on a spinning disk, allowing simultaneous acquisition of different points in the same image, which increases the acquisition speed. On the other hand, 2P excitation microscopy using two photons carrying half the energy required to excite the fluorescent molecule, can achieve high resolution optical sectioning due to the excitation point spread function (PSF). This is possible since the probability of two photons being absorbed simultaneously is extremely low, thus ensuring that two-photon fluorescence occurs only when the laser beam is precisely focused. As the laser beam focus must be moved on the desired region to obtain fluorescence, this technique is intrinsically a “scanning method”. In order to move the laser beam focus along the XY and Z axes, many systems have been developed. Most are mirror-based, but some examples of non-mirror-based scanners include electro-optic deflectors, using an electric field and an optical medium to deflect the laser beam, and acousto-optic deflectors, which rely on sound waves to change the laser beam’s direction.

Among mirror-based scanners, galvanometric and resonant mirrors are widely used in scientific research. Galvanometer scanners use mirrors mounted on fast-moving motors (galvanometers) to direct the laser beam onto the sample. Galvo mirrors rotate to specific angles based on the applied voltage, and the voltage can be modulated over time for precise control of the mirror's movement. A fast voltage changes results in fast mirror movement. However, due to the mirror and galvanometer's mass, achievable acceleration is limited by inertia, with a maximum scanning speed of around 1ms per line (0.5ms if data are acquired bidirectionally).

A galvo scanning module contains mirrors that rotate around axis orthogonal to each other, enabling full control over the scan in the XY axis. This allows several scanning options. In the linear scanning (Figure A) the laser moves in one direction along the X axis, achieving a scan speed of 2 frames per second (fps), while in the bi-directional scan the laser moves along the X axis in one direction for one line and in the opposite direction for the next line, achieving a scan speed of 4 fps.

Additionally, this system can acquire different regions of interest (ROIs) within the same field of view by moving along both the X and Y axes. This enables scanning through complex, 2-dimensional configurations (such as an oblique line, a rotated rectangle, a spiral, or any arbitrary pathway). Galvanometric systems can perform the **frame fly-to** and **frame fly-back** (Fig. 5) in approximately 0.5–1 ms, allowing rapid acquisition of multiple ROIs with minimal delay. Frame Fly-To is defined as the time taken to move the mirrors from the end of the last scanned pixel in one ROI to the first scanned pixel of the next ROI. Instead frame Flyback refers to the time required to move the mirrors from the last pixel of the final ROI back to the first pixel of the first ROI in the next frame.

This system allows for efficient and versatile scanning, making galvo systems suitable for applications that require fast and precise control of the laser beam. Conversely, resonant scanners utilize resonant mirrors that rotate at a fixed speed when voltage is applied, with the amplitude of the rotation depending on the applied voltage. These are used for very fast scanning (up to 67 µs per line in bidirectional mode) but can only rotate in one direction. Resonant scanners are often composed by a resonant mirror coupled with a galvanometric

one, where the resonant mirror moves the laser beam along the X axis, and the galvanometric mirror moves it along the Y axis.

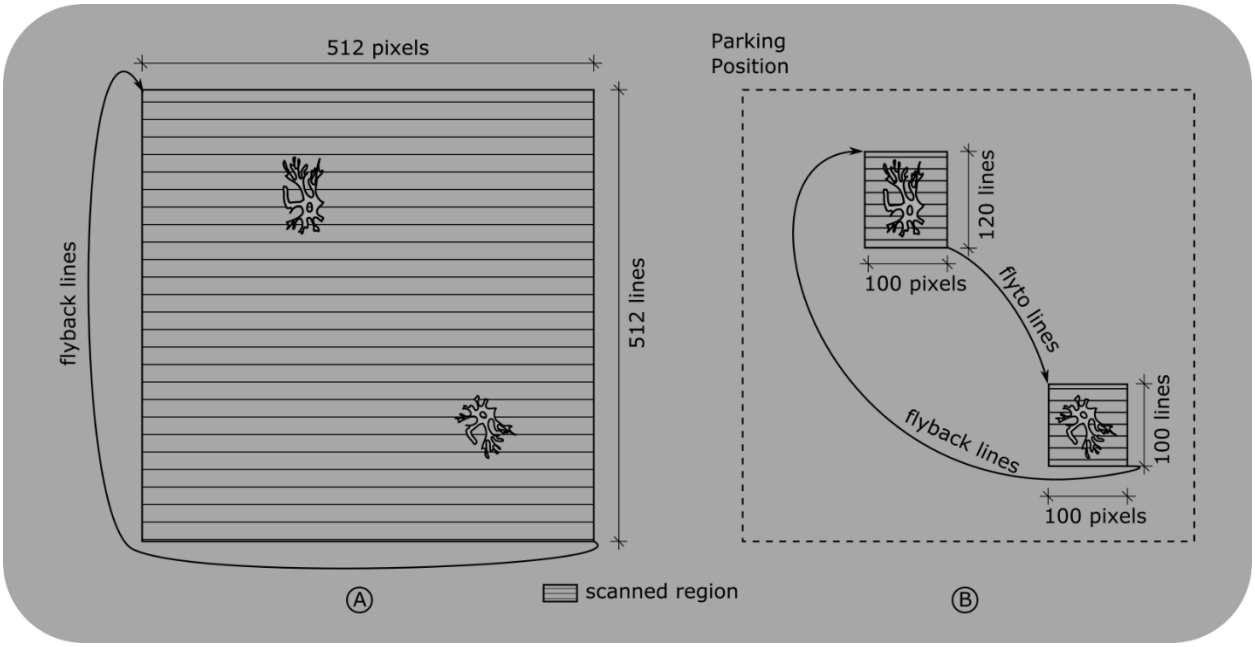

Figure 1.5. Scanning options with Galvanometric system
A. Linear scanning of the full field of view. Regions of low interest contribute to the frame period and therefore decrease the frame rate. B. Defining arbitrary ROIs the number of scanned lines is reduced, and the frame rate is maximized preserving image resolution (ScanImage Documentation, MBF Bioscience).

Techniques for single-spine calcium imaging

Dendritic spines are specialized structures are located in the postsynaptic terminal of excitatory synapses and protrude from the dendritic shaft. The most abundant dendritic spines have a mushroom shape, with a round head of approximately 0.5 μm in diameter and a thin neck that separates the spine's head from the parent dendrite. While the actual role of dendritic spine still remains unclear, most studies converge on a possible role of the thin neck to allow localized changes in response to synaptic activity (Yuste and Denk, 1995; Svoboda, Tank and Denk, 1996; Sabatini, Oertner and Svoboda, 2002).

On the membrane surface, dendritic spines contain glutamatergic receptors, such as AMPA and NMDA receptors, which are essential for excitatory neurotransmission. When glutamate is released by the presynaptic terminal, it binds to AMPARs and NMDARs on the postsynaptic

membrane. This local depolarization removes the magnesium block on the NMDA receptors, which further depolarizes the spine and allows calcium ions (Ca^{2+}) to enter. As dendritic spines depolarize, voltage-gated calcium channels (VGCCs) also activate, allowing additional calcium ions to enter. The influx of positive charges also contributes to dendritic depolarization. Inside the spine, calcium ions bind to various calcium-sensitive molecules, including Ca/Calmodulin-dependent kinase type II (CaMKII), which initiates biochemical signaling cascades that are crucial for neuronal activity and synaptic plasticity. Many calcium indicators have been developed based on calcium-binding molecules. These indicators are Ca^{2+}-sensitive molecules that allow the visualization of calcium accumulation within dendrites and spines. Currently, many synthetic calcium indicators are based on the backbone of the calcium-binding buffer 1,2-bis(o-aminophenoxy) ethane-N,N,N',N'-tetraacetic acid (BAPTA, Tsien, 1980; Minta et al., 1989). When BAPTA is attached to a fluorophore, the presence of calcium ions alters the fluorophore's photochemical properties. Specifically, the quantum yield (the efficiency of light emission) and the absorption cross-section (the likelihood of absorbing and emitting photons) change upon calcium binding (Higley and Sabatini, 2012).

Based on the same principle, different types of calcium sensors have been developed. These molecules vary in several aspects, including emission wavelength, efficiency of emission, calcium-binding affinity, and cell membrane permeability. This last feature influences the dye-loading techniques.

Depending on the type of calcium indicator, biological preparation, and scientific question, various methods can be used to load calcium indicators into cells.

Cell-membrane impermeant fluorescent indicators are the best choice for single-cell calcium imaging, which is ideal to analyze functional signaling in dendrites and spines. These indicators must be loaded cell-by-cell using sharp electrodes, single-cell electroporation, or whole-cell patch clamp, the gold standard for this type of experiment (Svoboda, Tank and Denk, 1996; Margrie, Brecht and Sakmann, 2002; Eilers and Konnerth, 2009).

Nevertheless, for network activity analysis, membrane-permeable acetoxymethyl (AM) ester calcium dyes are widely used (Grynkiewicz, Poenie and Tsien, 1985). These dyes can be released into the bath for ex vivo experiments or injected into brain tissue using air pressure pulses for in vivo experiments. Electroporation can also be used for AM dyes, where the dye is injected into a brain region, followed by trains of electrical pulses. This approach allows the dye to load into many neurons in the region of interest.

However, one major drawback of synthetic dyes is the difficulty of targeting specific cell types or subcellular compartments. Because of this limitation, genetically encoded calcium indicators (GECIs) have become widely used tools in neuroscience (Mank *et al.*, 2008). One of the most commonly used GECIs for in vivo experiments is GCaMP, consisting of a green fluorescent protein (GFP) fused to the calcium-binding protein calmodulin. In the presence of calcium, calmodulin triggers conformational changes in the fluorophore, leading to an increase of the emitted fluorescence. GECIs can be expressed in specific cell types by delivering the plasmid encoding the protein through viral transduction or in utero electroporation. For stable expression over long periods, it is also possible to create transgenic models that express GECIs in offspring ((Davidson and Breakefield, 2003). Since GECIs can be stably expressed in neurons (or other types of cells), they provide high expression levels over long periods with minimal adverse effects.

Capturing fast calcium transients induced by synaptic activity requires imaging techniques with high temporal resolution, such as two-photon scanning microscopy. Choosing the appropriate calcium indicator is critical for single-spine imaging. Both synthetic and genetically encoded calcium indicators have their advantages.

Synthetic indicators generally offer higher signal-to-noise ratios and faster kinetics in addition to a higher affinity for calcium, with dissociation constants (Kd) around 400–500 nM. Conversely, GECIs provide stable, long-term expression and cell-type specificity, making them an ideal choice for chronic studies.

Use of optogenetics for interrogating neural circuits

Optogenetics is a powerful and widely used technique in neuroscience, enabling the control of neuronal activity using light to manipulate the activity of specific targeted neurons (Zemelman *et al.*, 2002; Boyden *et al.*, 2005; Nagel *et al.*, 2005). This technique relies on the expression of opsins, ion channels derived from microorganisms sensitive to different light wavelengths (Yizhar *et al.*, 2011). Among these channels there are channelrhodopsins (ChR), halorhodopsins, and archaerhodopsins. ChR, typically activated by blue light (~470 nm), is a cation channels that lead to neuronal depolarization and excitation (Boyden *et al.*, 2005). Conversely, halorhodopsins and archaerhodopsins, activated by yellow or green light (~590 nm), induce neuronal hyperpolarization by allowing chloride ions to enter or protons to exit, respectively, silencing neuronal activity (Zhang *et al.*, 2006). The expression of opsins is typically achieved through genetic manipulation, often using viral vectors like adeno-associated viruses (AAVs) or by creating transgenic animals. These vectors carry plasmids containing opsin genes, placed under specific promoters to ensure expression in targeted neuronal populations (Madisen *et al.*, 2012). Once expressed, light of a specific wavelength can be used to control neuronal activity, both *in vitro* and *in vivo*.

Optogenetics is particularly valuable for mapping neural circuits. By selectively activating or inhibiting specific neurons, it is possible to delineate functional connections between different brain regions (Felix-Ortiz and Tye, 2014). ChRs are typically expressed throughout the neuron, including the soma, dendrites, and axon terminals, permitting precise control over different neuronal compartments (Cruikshank *et al.*, 2010). When light is applied to axonal terminals, the channel's activation causes an influx of cations, leading to depolarization and neurotransmitter release (Hamada *et al.*, 2021). This local release can modulate synaptic activity and influence downstream neurons.

ChR expression combined with electrophysiology or calcium imaging offers powerful tools for mapping long-range projections and local circuits (Petreanu *et al.*, 2007). For instance, optogenetic stimulation of a specific brain region coupled with patch-clamp recordings or calcium imaging in the projecting area, allows to study neural projections and functional connectivity in detail (Madisen *et al.*, 2012). *In vivo* experiments can target either the cell

bodies or axon terminals, each providing insight into distinct scientific questions (Yizhar *et al.*, 2011). For example, causal relationships between the activity of optogenetically targeted cell bodies and behavioral outcomes can be established by modulating their firing rates during behavioral assays. This manipulation enables the investigation of how changes in neuronal activity influence specific behaviors, providing direct evidence of the role of the targeted cells in the observed outcomes. In contrast, targeting the axon terminals allows for a more detailed understanding of specific neural pathways' connectivity and functions. Optogenetic manipulation of axon terminals is particularly useful in *ex vivo* studies of long-range projections, where controlling terminals enables precise exploration of these connections, enhancing our understanding of complex neural networks (Tye *et al.*, 2011).

Research Objective

The spatial organization of synaptic inputs plays a pivotal role in shaping dendritic integration, yet a comprehensive understanding of their arrangement across the entire dendritic tree of pyramidal neurons remains elusive. While anatomical approaches, such as GFP reconstitution at synapses, offer detailed maps of synaptic contact distribution, they lack the ability to identify functionally active inputs. Conversely, functional imaging methods, such as calcium or glutamate imaging, have been limited to small dendritic regions, leaving the broader organizational principles unexplored. In this study, we address this critical gap by employing two-photon laser scanning microscopy to perform calcium imaging at the level of individual glutamatergic spines throughout the dendritic tree of pyramidal neurons in the CA1 region of the ventral hippocampus (vCA1 PNs). By focusing on inputs from the basolateral amygdala (BLA) and CA3 (Schaffer Collaterals, SC)—two projections converging onto apical proximal and basal dendrites—we provide a novel and integrative perspective on how spatial synaptic organization might influences dendritic integration, offering insights into both anatomical and functional dimensions of synaptic activity.

2. Methods

Animals

All animal care and experimental procedures were conducted in accordance with Istituto Italiano di Tecnologia (IIT) licensing as well as the Italian Ministry of Health (D.Lgs 26/2014) and EU guidelines (Directive 2010/63/EU). The experiments were conducted on Fos-TRAP2 ($Fos^{tm2.1(iCRE/ERT2)Luo/J}$, Jackson laboratory, USA) mice. Male and female inbred Fos-TRAP2 mice were housed in filtered cages, in a climate-controlled animal facility (22 ± 2°C) and maintained on a 12-hour light/dark cycle with water and food ad libitum. Animals were bred in IIT.

Surgical procedures

Mice of either sex aged 5 to 7 weeks were used for stereotaxic injection of Adenoassociated virus (AAV). Animals were first weighted and checked for overall health status. Subsequently, they were positioned for 3 minutes in the anesthesia chamber with isoflurane (4%) and 95% oxygen (1.5 L/min). Mice were then mounted on the stereotaxic frame while maintaining anesthesia using 2% isoflurane and oxygen (0.8L/min). Injection of ketorolac (5-7.5 mg/kg) and enrofloxacin (5 mg/kg**)** was provided intraperitoneally as analgesic and antibiotic, respectively. During the surgery, the temperature was maintained at 37°C by using a feedback-controlled heating pad and ophthalmic ointment was applied to avoid eye drying. For ex-vivo optogenetic stimulation of amygdalo-hippocampal projection, a small craniotomy was performed over the cortex with a dental drill. AAV-CaMKII-hChR2-EYFP (>10^13 vg/ul, Addgene: # 26969-AAV5) was injected bilaterally in BLA (stereotactic coordinates: AP +1.6, ML: ±3.32, DV: +4.90) through a glass pipette attached to a Hamilton syringe (Model: 1701RN) at a rate of 100 nl/min controlled with a microinjection syringe pump (UMP3, world precision instruments, Sarasota, FL, USA). The injection syringes were

left in place for 10 minutes before withdrawal. Mice were then monitored for two days post-surgery to ensure proper recovery.

Slice preparation

Four to six weeks after AAV injections, mice were deeply anesthetized by injecting intraperitoneally an overdose solution of ketamine (200mg/kg) + xylazine (20mg/kg). Then, they were transcardially perfused with an ice-cold N-methyl-D-glucamine (NMDG) based solution containing (in mM): 92 NMDG, 2.5 KCl, 1.25 NaH_2PO_4, 30 $NaHCO_3$, 20 HEPES, 25 glucose, 2 thiourea, 5 Na-ascorbate, 3 Na-pyruvate, 0.5 $CaCl_2 \cdot 2H_2O$, and 10 $MgSO_4 \cdot 7H_2O$, pH adjusted to 7.3-7.4 with 5M hydrochloric acid and equilibrated with 95% O_2 and 5% CO_2. Brains were extracted and submerged in ice-cold NMDG cutting solution. Horizontal brain slices (350 µm thick) were prepared from either hemisphere in ice-cold NMDG-cutting solution using a vibratome (VT1200S, Leica Microsystems), incubated in a maintenance chamber at ~35 °C for 20/30 minutes in the NMDG-cutting solution, and subsequently stored at room temperature (RT) in artificial cerebrospinal fluid (ACSF). The ACSF solution contained (in mM): 125 NaCl, 26 $NaHCO_3$, 2.5 KCl, 1.25 NaH_2PO_4, 10 glucose, 2.3 $CaCl_2$, and 1.3 $MgCl_2$, equilibrated at 95% O_2 and 5% CO_2 for at least 40 minutes.

Electrophysiological recordings

After at least 1h of recovery in ACSF at RT, the slices were transferred to the recording chamber and constantly perfused with RT ACSF (2ml/min). Patch pipettes were prepared using a horizontal puller (P-1000 Next Generation Micropipette Puller, Sutter Instrument) from borosilicate glass capillaries (Warner Instruments, LLC, Hamden, USA). When filled with a K-gluconate-based intracellular solution, the pipettes had a resistance of 4 to 6 MΩ. The composition of the intracellular solution was as follows (in mM):135 K-gluconate, 5 KCl, 2NaCl, 10 Na2P-Creatine, 0.1 EGTA, 10 Hepes, 5 Mg-ATP, 0.4 Na-GTP (280~300 mOsm, adjusted to pH 7.2 with KOH). In addition, intracellular solution contained Alexa-Fluor 594

(75µM, ThermoFisher #A10438) to visualize dendritic arborization and the synthetic calcium indicator Fluo-5F Pentapotassium Salt (300µM, ThermoFisher #F14221). Brain slices were visualized with a Dodt Gradient Contrast (DGC) microscope (Scientifica hypercope) in bright field using a UV filter paired with an oil-condenser (Olympus U-AAc), using a 16X objective (Nikon, 0.8W, 3.0mm WD). Whole-cell cell configuration was reached in identified and selected pyramidal neurons in ventral CA1. The cell was maintained for at least 10 minutes in voltage-clamp at -70 mV. Then, in the current clamp configuration, we injected 500ms long current steps to assess the neuronal electrophysiological activity. For Schaffer collateral stimulation, an Ag/AgCl electrode was introduced in an ACSF-filled glass pipette. The stimulator pipette was placed ~300µm from the patched cell in the stratum radiatum. To elicit a synaptic response, we delivered two stimuli (~0.8ms long) 50ms apart (20Hz) to reduce synaptic failures. The amplitude of the current stimulus was adjusted by using an isolated constant current stimulator (Digimiter Ltd.) to elicit a minimal synaptic response.
For channel Rhodopsin stimulation, single 2ms long LED pulse at 470nm with an intensity of ~3-7mW (measured below the objective) was provided by using a CoolLED's pE-300^{white} as light source paired with a GFP filter (SCI-49002s, Scientifica, UK).
Currents were sampled at 10 KHz and digitally filtered at 3 KHz using the 700B Axopatch amplifier (Molecular Devices, Sunnyvale, CA).

Two-photon images acquisition

Prior to two-photon imaging, a 20-minute period was allowed for Alexa and Fluo-5F to diffuse throughout the dendrites. Imaging was conducted using a tunable titanium-sapphire laser (Chameleon, Coherent) set to 810 nm, with power levels of approximately 6–11 mW measured below the objective. A 1024x1024 pixel Z-stack image of Alexa Fluor was acquired, with planes spaced approximately 1–1.5 µm apart. The neuron's structure was then semi-automatically traced using the Simple neurite tracer (SNT) plug-in in Fiji, and each traced dendrite was manually classified as either apical or basal. The resulting data was exported as an .swc file, which was subsequently processed by a custom Python script to create

regions of interest (ROIs) for automated placement, as described in the following section. ScanImage was used to control the two-photon scanning system for calcium imaging. The software was used to control the two-photon scanning microscope, which operates in a galvo-galvo configuration. This setup allowed for precise control over various imaging parameters, including laser scanning, image acquisition, and focusing, enabling high-resolution imaging of calcium signals with fine spatial and temporal control. The galvo-galvo configuration ensures rapid scanning and accurate imaging of dendritic spines in the ROIs.

Automatic ROI drawing and placement

A Python-based algorithm was developed to automate ROI placement across the identified neuron. First a .swc file containing the 3D location information (x, y, z) for each neuronal segment is converted into a .roi file compatible with the ScanImage software. The .swc file is generated through the semi-automatic tracing of neuronal backbones in the SNT plug-in of the FIJI software. In the SNT output file, the neuron is represented as a series of connected nodes, starting from the soma, represented as a single node. Dendrites connected to the soma are manually classified as either apical or basal based on their position relative to the soma. Dendrites extend from the soma as a hierarchical network of interconnected branches. The main branches originating directly from the soma are called primary dendrites. These primary dendrites give rise to secondary dendrites, which branch out from the primary dendrites at specific nodes, called “fork points”. Similarly, tertiary dendrites emerge from branch points along the secondary dendrites. This branching forms a tree-like structure, with each branch connected in a parent-child hierarchy. Secondary dendrites are the "children" of the primary dendrites, and tertiary dendrites are the "children" of the secondary dendrites. Nodes are automatically categorized by their z-layer (depth) to enable the identification of contiguous segments within the same spatial plane. The Python algorithm identifies contiguous nodes within each z-layer, classifying the ‘close node’ as the one nearest to the soma and the ‘far node’ as the one farthest from the soma. A minimum number of contiguous nodes per z-layer is required for consideration. If the chain meets this

threshold, a rectangular ROI is generated around the nodes, with the close and far nodes positioned at the midpoints of the two parallel sides. The rectangle's length is determined by the number of consecutive nodes, extended by 10% in both directions, while the width remains fixed. The system then verifies that all nodes fit within the rectangle width; if not, the rectangle is resized accordingly. Each z-layer may contain zero, one, or multiple rectangles. To ensure a consistent frame rate across z-planes, the algorithm considers factors such as frame rate, the time required for galvos to move between ROIs (the 'flyto' and 'flyback' times), and pixel dwell time. Each ROI is filled with pixels according to these parameters. Given that ROI number and dimensions vary across z-planes, the pixel count within each ROI is adjusted to maintain the frame rate while ensuring a spatial resolution of at least 3.8 pixels per micron. This requirement is based on the optical system's diffraction-limited resolution, calculated at 0.56 µm using the Abbe diffraction limit. Following the Nyquist criterion for minimum sampling density, at least two pixels per 0.56 µm are needed to accurately sample the signal, resulting in a target density of 3.8 pixels per micron.

The Abbe diffraction limit, *d*, is calculated as:

$$d = \frac{\lambda}{2\,NA}$$

where λ represents the wavelength of the imaging light, and NA the numerical aperture of the objective. According to the Nyquist criterion, the sampling frequency (f_s) should be at least twice the maximum spatial frequency (f_{max}) to properly sample all spatial details:

$$fs \geq 2 \cdot fmax$$

Once obtained the information about the dimension, the position, the rotation, and the number of pixels of each rectangle, these data are stored in a .ROI file that is readable by ScanImage. Each .ROI file was sequentially uploaded to the software, after which the operator manually adjusted the focus to ensure that all the ROIs in the z-plane were properly imaged. Once the correct focus was set, the stimulation protocol was executed to induce the desired synaptic activity while maintaining optimal imaging conditions.

Two-photon calcium imaging

For two-photon calcium imaging, the slices were perfused with 0 Mg^{2+} ACSF containing Picrotoxin (50 µM) to block GABAR-mediated inhibition and D-serine (10µM) to enhance NMDA receptors activity while clamping neurons at -70mV. Each z-plane was imaged independently, and each plane contained a scan field with all the ROI. The protocol consisted of two acquisitions of 50 frames at 16Hz. The first acquisition provides one LED stimulus (2ms) to optogenetically induce glutamate release in Basolateral Amygdala (BLA) terminals. Five seconds later, during the second acquisition, Schaffer collateral discharge was induced by providing a paired-pulse stimulation (two stimuli at 20 Hz). The entire protocol was repeated 5 times for each z-plane at a frequency of 0.1 Hz.

DeepD3 based semantic segmentation

DeepD3 is an open-source, deep learning-based framework designed for the automated identification of dendritic spines ((Fernholz *et al.*, 2024)). It operates using a supervised learning approach with a convolutional neural network (CNN), a computational model optimized for processing grid-like data, such as images. The network is termed 'convolutional' because the initial layer typically applies a filter (or convolution) to the input to extract features such as edges and textures. With additional layers, the model progressively learns more complex features of the input image. Following each convolution, an activation function, such as ReLU (Rectified Linear Unit), introduces non-linearity, enhancing the model's capacity to learn intricate patterns. In this framework, labeled images are used to train the model to recognize specific features, making it a supervised learning approach.

To enhance DeepD3's performance in identifying dendritic spines under specific experimental conditions, the model was trained using maximum intensity projections of the Alexa Fluor signal across 50 frames for each ROI image. A training dataset was created by manually annotating dendritic spines with pixel-level precision using the Napari software.

Once the model demonstrated consistent accuracy, a complete set of ROIs was provided to enable effective reconstruction of dendritic spines along the dendritic tree.

Calcium signals detection

DeepD3 was used for automatic spine segmentation obtaining the number and position of detected spines. The machine learning model generated masks for each dendritic spine and we calculated the mean of the fluorescence intensities of all pixels within each mask for each frame and generated a time series of the fluorescence for individual spines. Then we calculated ΔF/F as follow:

$$\frac{\Delta \mathrm{F}}{\mathrm{F}} = \frac{F(t) - F_0(\mathrm{t})}{F_0(\mathrm{t})}$$

Where F(t) is the average fluorescence of the pixel in each spine mask at time t, and $F_0(\mathrm{t})$ is the baseline fluorescence computed as the 10th percentile of the average fluorescence intensity in a 500 ms-long rolling window centered in t. Subsequently, ΔF/F traces were filtered by applying a modified the Okada filter (Fig.1, Ishikawa *et al.*, 2020). To differentiate signal from noise, filtered traces were standardize by calculating the Z-score:

$$Z = \frac{x - \mu}{\sigma}$$

where x is the observed value, μ is the mean of the value and σ is the standard deviation. To identify traces exhibiting calcium events, 2781 traces were randomly sorted and manually labelled to distinguish signal to noise (2578 labeled as non-events "0" and 203 labeled as containing events). The sorted traces were divided into three datasets: training dataset, validation and a test each of them containing 50 %, 25% and 25% of the traces maintaining the proportion between noise and signal using a weighted random sampler. Then a neural network was instructed to recognize events. We employed a custom 1D convolutional neural network that comprises two convolutional layers (16 and 32 filters, respectively, with a kernel size of 3), each convolutional layer is followed by a ReLU activation function to

introduce non-linearity, enabling the model to learn complex patterns in the data. Dropout regularization (50%) is applied after the first and second layers to reduce the risk of overfitting by randomly deactivating a fraction of the neurons during training. After the second convolutional layer, a max-pooling layer with a kernel size of 2 is used to downsample the feature maps, reducing their size and highlighting the most prominent features. The resulting output is then flattened into a one-dimensional vector, which is passed through a fully connected (dense) layer with 64 units to combine features. Finally, the output is fed into a single-unit binary classification layer with a sigmoid activation function, which produces a probability score indicating the presence of an event. The network produced a probability distribution representing the likelihood of an event in each trace. To classify traces as containing an event, a threshold at the 99th percentile ($p < 0.01$) was applied, converting the probability distribution into a binary outcome. This threshold ensured high specificity, confidently identifying traces with significant calcium activity.

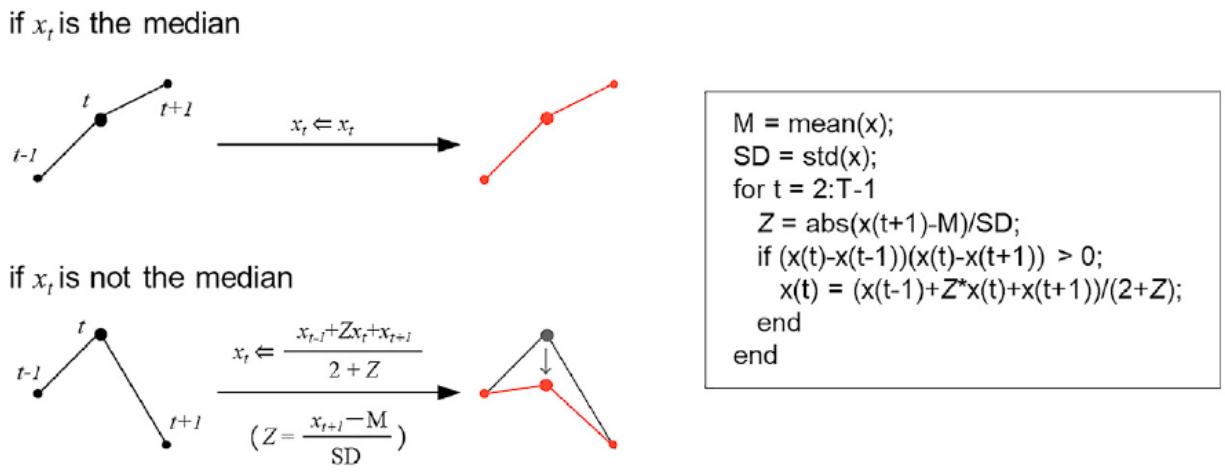

Figure 2.1. Modified Okada filter

Diagram of the data processing method using an adapted Okada filter (left). At a given time point t, fluorescence intensity is evaluated in comparison with the values at the immediately preceding, X_{t-1}, and following, X_{t+1}, time points. If X_t is the median of X_{t-1}, X_t, X_{t+1} — meaning $(X_t - X_{t-1})$ $(Xt - X_{t+1}) \leq 0$ then X_t remains unchanged (top panel). Otherwise, if X_t is not the median, X_t is replaced by $(X_{t-1} + ZX_t + X_{t+1})/(2+Z)$ (bottom panel). Here, the coefficient Z is calculated as $(X_{t+1}-M)/SD$, with M representing the mean and SD the standard deviation of the entire time series $\{X_t\}$ (Adapted from Ishikawa et al., 2020).

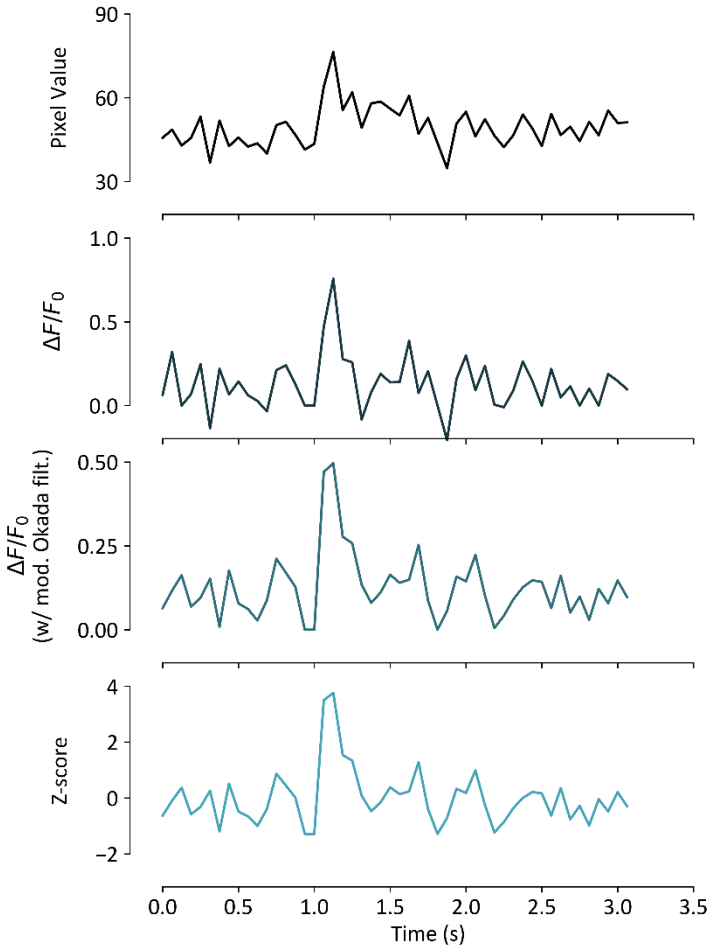

Figure 2.2. Processing pipeline for denoising

The figure illustrates the steps involved in denoising a time series generated by calculating the mean fluorescence intensity of all pixels within a mask for each frame. The top trace shows the raw pixel values. The second trace represents the $\Delta F/F_0$ calculation using a rolling window centered at time t. The third trace shows the $\Delta F/F_0$ after applying the modified Okada filter. The bottom trace represents the Z-score of the $\Delta F/F_0$ following the application of the Okada filter. This Z-score is subsequently used as input to the classifier to determine whether each event is classified as an "event" or "no event."

Analysis of spine distribution

For each experiment quantifications and statistical details (statistical significance and test used) can be found in the main text and figure legends. Data and statistical analyses were conducted using Python. The Shapiro-Wilk test was applied to assess normality. For normally distributed datasets, comparisons were made using a T-test, while non-normally distributed datasets were analyzed using a two-tailed non-parametric Mann-Whitney U-test. To evaluate statistical differences within branches, equal variance was first assessed with Levene's test. If equal variance was confirmed, a one-way ANOVA was performed, followed by Tukey's multiple comparison test. For datasets that did not meet the equal variance criterion, the Kruskal-Wallis test was used, followed by Dunn's non-parametric pairwise multiple comparison test.

To investigate branch-to-branch variability, the activation of spines was modeled as a binomial process assuming a uniform activation probability (p) across all spines of the neuron. Each spine on a branch was treated as an independent trial, where the probability of activation was set equal to the neuron-wide activation frequency. This allowed us to define a null hypothesis: that the number of activated spines on a branch (k) follows a binomial distribution $B(n,p)$, where n represents the total number of spines on the branch. The observed number of activated spines (k) on each branch was compared to the expected binomial distribution for branches of the same size (n). For each branch, the probability (p-value) of observing k or more activated spines was calculated under the null hypothesis. A two-sided p-value was calculated to check for deviations from the expected probability p in both directions.

3. Results

Automated ROI Placement for High-Precision Spine Calcium Imaging Across Dendritic Trees

As mentioned above, many studies investigating dendritic synapses typically focus either on synaptic function at the level of individual dendritic branches or map synaptic distribution at whole-neuron level. In the present study we sought to explore the glutamatergic spine activity across the entire neuronal tree with the aim to understand how diverse inputs are functionally compartmentalized. In particular, we investigated the functional spatial organization of both CA3 (Schaffer Collaterals) and BLA synaptic inputs onto the dendritic tree of ventral CA1 pyramidal. To this end, we first filled neurons with Alexa Fluor 594 through the patch-clamp recording pipette enabling to visualize the precise morphology of the dendritic neuronal backbone and with the synthetic calcium indicator Fluo-5F. This configuration allowed us to perform two-photon Ca^{2+} imaging at the level of the single dendritic spine thus monitoring the synaptic activity and localization with microscale precision. Capture the rapid dynamics of single-spine Ca^{2+} transients required a frame rate of ~ 16 Hz. However, due to the intrinsic limitations of our 2P system, scanning a full z-layer at this rate would have reduced the imaging resolution thus making it difficult to resolve the smaller regions of interest at individual spines within the field of view. To optimize temporal resolution without sacrificing spatial details, we chose to image only selected regions of interest (ROIs) within each z-layer, by specifically targeting areas containing dendritic branches. By using this approach, we were able to image the regions of interest (ROIs) at the desired frame rate while maintaining sufficient spatial resolution. We initially used the strategy to identify and image single ROI comprising dendrites along their entire length. However, this method presented several limitations when aiming to capture the entire dendritic tree. First, it was highly error-prone, as it relied on the operator to draw the ROI and choose the scanning order of the different ROIs increasing the risk of scanning specific ROIs twice or other the be missed. Additionally, manually selecting dendritic ROIs was time-

consuming and often led to inconsistent ROI placement order. To address these issues, we implemented a systematic approach by dividing the neuron into multiple z-layers and targeting each layer individually. Although this improved the ROIs identification, the manually drawing ROIs for each z-layer still was labor-intensive and error-prone. To simplify this process and improve accuracy, we developed an automated Python algorithm to place ROIs on the dendritic structure traced with Alexa Fluor 594 in an unbiased and operator-independent fashion. This method allowed for precise ROIs placement across z-layers, significantly enhancing both the efficiency and reliability of our imaging protocol. After filling the neuron through the patch pipette, we acquired the z-stack (Fig. 1A) and reconstructed the neuronal structure (Fig.1B) by using the Simple Neurite Tracer (SNT) plugin in the FIJI software. Next, our algorithm processed the FIJI-generated file (see methods) and created ROIs for each z-layer, precisely aligning them with the dendritic portions to cover the whole dendritic arbor (Fig.1C). To consistently acquire each z-plane, we designed our algorithm to create the ROIs maintaining a fixed frame rate throughout z-planes. Since the dimensions and number of ROIs within each z-plane can vary (Fig 1C), the algorithm dynamically adjusts the pixel count to ensure optimal resolution while maintaining the fixed frame rate along z-planes. To meet the resolution needs of our diffraction-limited optical system, which has a calculated resolution limit of 0.56 µm (determined by the Abbe diffraction limit, d), we set a minimum sampling density of 3.8 pixels per micron. This criterion is derived using the Nyquist sampling theorem, which requires, in our conditions, a minimum of two pixels per 0.56 µm to accurately sample the image signal. In this way, each ROI captured fine structural details at a minimum density of 3.8 pixels per micron, ensuring both spatial and temporal resolution across the z-stack. However, our ROIs typically exceed this minimum pixel density, providing finer detail in the acquired images.

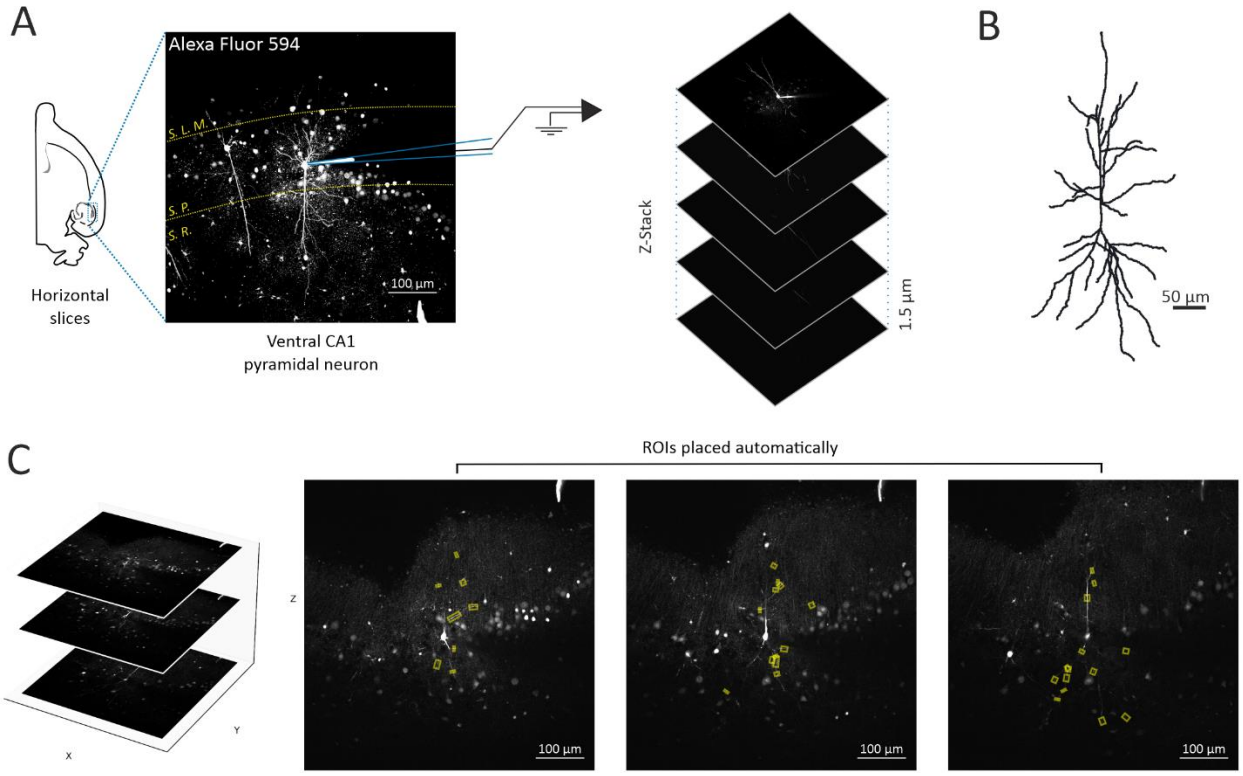

Figure 3.1. Automatic ROIs placement on Z-layers

A) Horizontal acute brain slice was selected to contain ventral hippocampus. The image shows the maximal projection of the z-stack of a CA1 pyramidal neuron patched and filled with intracellular solution containing a fluorescent tracer (Alexa Fluor 594). S.L.M. (strato lacunosum moleculare), S.P. (stratum piramidale), S.R. (stratum Radiatus). On the right, A Z-stack with an interlayer distance of 1.5 µm was acquired to image the entire structure of the neuron. B) 3D reconstruction of the patched neuron obtained by using semi-automatic tracing. C) Using information about the neuronal structure, the ROIpy custom algorithm placed ROIs on each Z-layer. On the left side, a portion of a z-stack as example, on the right side the three layers are shown individually, and ROIs are shown as yellow box on each layer.

Combined Optogenetic and Electrical Stimulation to Characterize BLA and SCs Synaptic Inputs

To assess the functional profile of synaptic connections between the Basolateral Amygdala (BLA) and CA1 pyramidal neurons in the ventral hippocampus, we injected AAV5-CaMKII-ChR2-EYFP into the BLA of Fos-TRAP2 mice, enabling optogenetic stimulation of BLA synaptic terminals that target the dendritic trees of CA1 neurons.

As mentioned above, CA1 pyramidal neurons in acute brain slices were loaded with Fluo-5F (300μM) and the red fluorophore Alexa Fluor 594 (75μM) through the patch pipette. Both fluorophores were efficiently two-photon excited at wavelengths of λ = 810 nm: Alexa Fluor 594 fluorescence provided structural detail, while Fluo-5F allowed us to detect and measure Ca^{2+} influx in response to synaptic activation. We stimulated BLA terminals with a single LED pulse (470 nm, 2ms) and induced Schaffer collateral activation with a paired-pulse electric stimulation (20 Hz) using an electrode placed ~300 μm away from the patched cell in the stratum radiatum (Fig. 2A). The delivery of a paired pulse was intended to increase the probability of release of Schaffer collateral terminals with respect to single pulses. This approach enabled us to reliably observe excitatory postsynaptic currents (EPSCs) evoked by either Schaffer collateral (SC) or basolateral amygdala (BLA) inputs across multiple patched neurons. Additionally, we observed Ca^{2+} influx in response to these two distinct synaptic inputs, thus detecting synaptic activity with a high spatial resolution (Fig. 2B). During the imaging session a single scan field (that is the sum of all the ROIs in a single z-layer) was acquired 5 times at 0.1Hz. In each acquisition, we applied optogenetic and electrical stimulation with a 5-second interval to clearly distinguish the source of synaptic activation and prevent integration of the two inputs (Fig. 2C). During optogenetic stimulation, the gated photomultiplier tubes (PMTs) were turned off for 5 ms to prevent interference from the LED signal and to protect the PMTs. To maximize the Ca^{2+} influx through NMDARs in dendritic spines, we conducted experiments in ACSF 0M of magnesium (Mg^{2+}) and supplemented with D-serine. In addition, GABA receptors were blocked with picrotoxin to prevent inhibitory effects, and AMPA receptors were blocked with CNQX to ensure that the glutamate released

into the synaptic cleft primarily interacted with the NMDARs binding sites. In these conditions, the time needed for the dialysis of ALEXA594/Fluo-5F together with the scanning/imaging of each z-layer, depending on the number of z-layers (Fig. 2D), could take up to three hours. Although maintaining patch stability throughout the imaging sessions posed a significant experimental challenge, we managed to successfully scan nearly the entire dendritic arbor of 7 neurons.

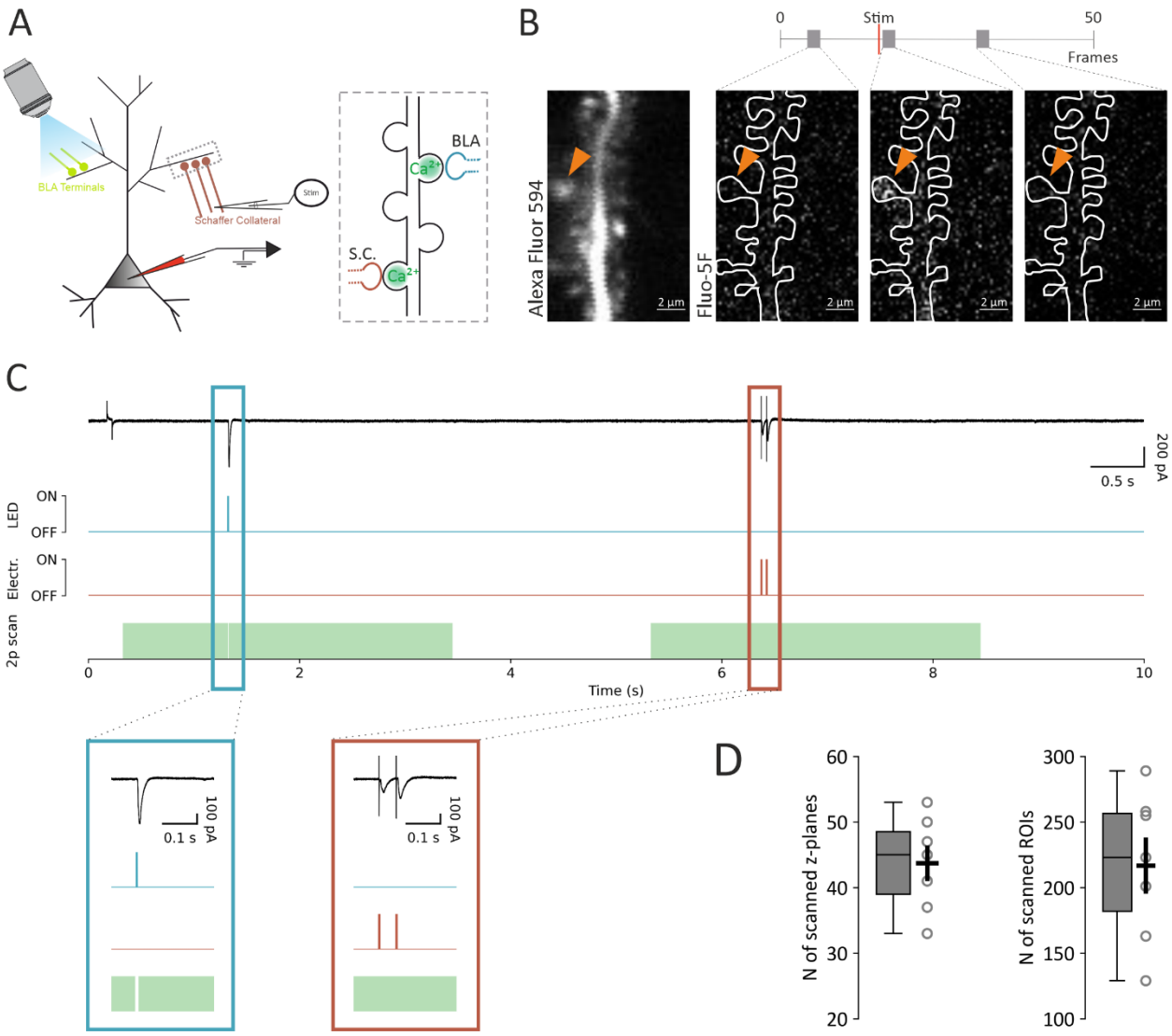

Figure 3.2. BLA and SCs stimulation protocol to scan neurons across many z-layers
A) A cartoon illustrating a patched neuron in which BLA terminals are stimulated using optogenetics, while Schaffer collateral (SC) fibers are activated by electrode placement in the stratum radiatus. On the right, a portion of the dendrite is shown with its spines, where calcium influx could be induced by synaptic activity from either the BLA or SC.
B) On the left, a single ROI shows a dendritic portion labeled with Alexa Fluor 594. On the right, a representative calcium transient in a dendritic spine is displayed within the ROI. The three frames of the Fluo-5F signal represent different moments of the imaging session: the first taken five frames after the start, the second immediately after the optogenetic or electric stimulation, and the last one taken 10 frames post-stimulus (frame rate 16 Hz). The orange arrowhead indicates the spine where Fluo-5F fluorescence intensity increases, signifying calcium influx.
C) A representation of the different output channels during a single recording: in black, the current recorded by the patch pipette; in blue, the LED trigger for optogenetic stimulation; in red, the stimulus for electric paired pulse; and in green, the scanning period.
D) On the left, the number of z-planes in the z-stack that are acquired. On the right, the total number of ROIs needed to scan the neurons.

Automated Detection and Spatial Analysis of Dendritic Spines in CA1 Pyramidal Neurons

To create the precise map of synaptic activity, each spine was associated with a specific location on the dendritic tree, and the detection of calcium transients at spines was considered as a proxy of synaptic activation. Typically, we scanned approximately 200 ROIs for each neuron (Fig 2D, right panel). Similarly to the above-mentioned placement of ROIs in the neuronal dendrites, the manual labeling of each dendritic spine within these ROIs was error-prone and time-consuming. As in the previous case, we decided to automatize this procedure by using a published deep learning-based framework offering the possibility to detect and identify dendrites and dendritic spines (Fernholz *et al.*, 2024, see methods). This neural network performed semantic segmentation across all acquired ROIs, robustly individuating and quantifying dendritic spines (Fig. 3A). The process enabled us to generate an initial map that outlined the position of all identified spines throughout the scanned dendritic tree (Fig. 3B). We found that, overall, more spines were identified in the apical region. However, after normalizing the number of detected spines by dendritic length in both apical and basal compartments, we concluded that the higher spine count in the apical area likely reflects its greater representation within the neurons we scanned (Fig. 3C). Moreover, we observed a moderate positive correlation ($r = 0.54$) between dendritic length and spine number, confirming that longer dendrites generally showed a higher number of spines (Fig. 3D). We also considered independently the two dendritic compartments, and the correlation between dendritic length and spine number increased in both cases: 0.62 for apical dendrites and 0.77 for basal dendrites.

We further categorized neuronal compartments by dividing dendrites in branch degrees (Fig. 3E). We found that the number of spines on different branch types were not equally represented, showing differences among groups but no differences in pairwise comparison. Then, since segmented spines in apical and basal compartment resulted to be not equally represented (Fig. 3C), we further divided neuronal compartments into their relative branch degrees and tested them for differences. Due to their limited representation in this dataset,

we excluded fourth-degree branches from the analysis. Comparison between dendrites sorted from the apical compartment showed denser spines in the third-degree respect to the first-degree(Fig. 3F).

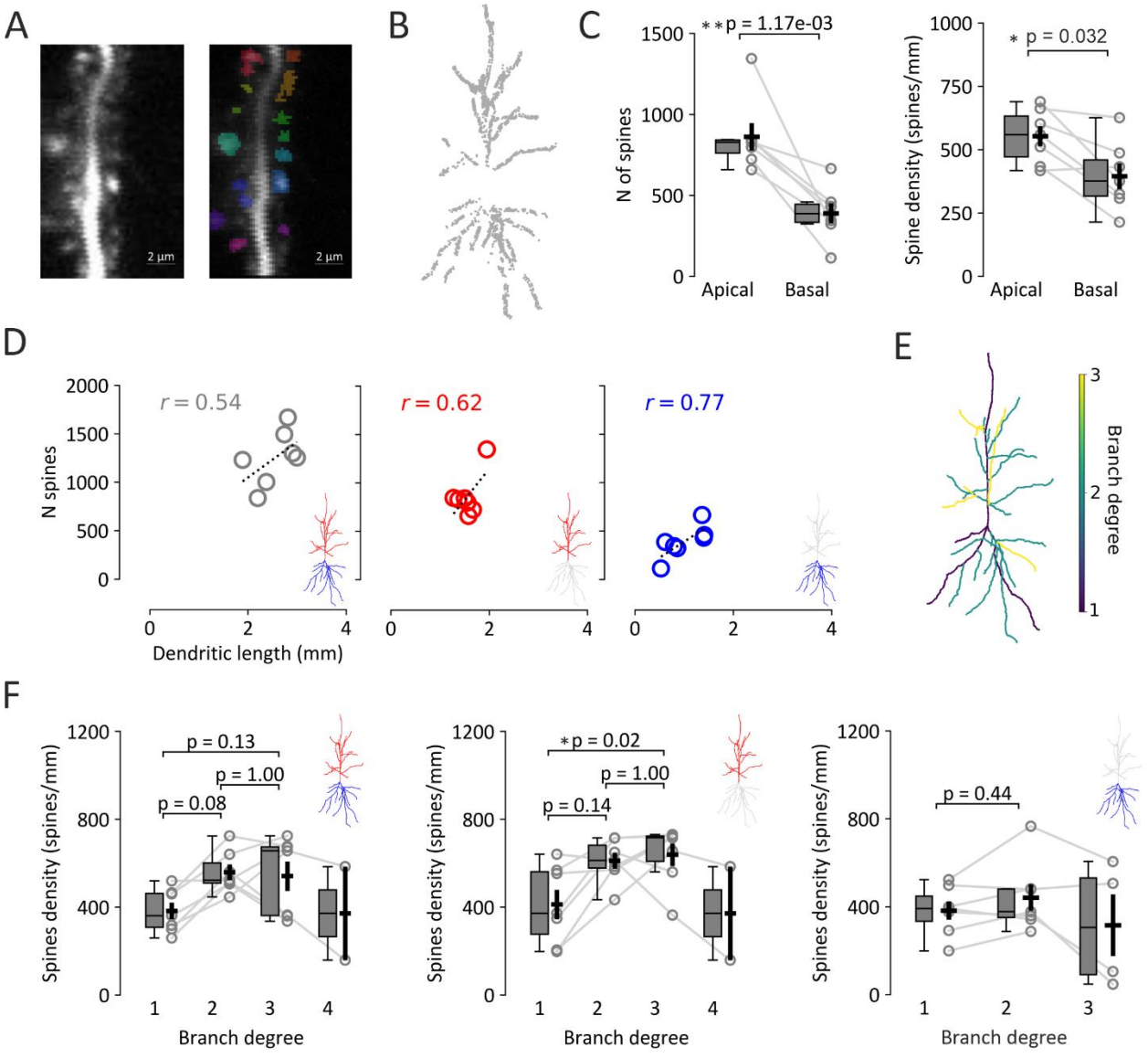

Figure 3.3. Automatic spines detection on the dendritic tree

A) Left: An example image showing a region of interest (ROI) with a dendritic portion filled with Alexa Fluor 594, a fluorescent dye for visualizing neuronal structures. Right: The same dendritic portion processed by the DeepD3 algorithm, which automatically recognizes and segments dendritic spines. Each colored mask represents an individual segmented spine.

B) Complete map of all spines automatically recognized and rearranged to reflect their positions along the dendrite, reconstructing the shape of the neuron.

C)Left Plot: Comparison of the number of spines segmented by the model in the apical and basal compartments (n=7 neurons, p = 0.0011, Mann-Whitney U test).

Right Plot: Number of spines in each compartment normalized by the total dendritic length of that compartment, providing a measure of spine density (n=7 neurons, p = 0.032, T-test). Each small circle represents an individual neuron, with lines connecting paired measurements from the same neuron in the apical and basal compartments.
Box Plot Details: The black cross represents the mean ± SEM. The box spans the interquartile range (IQR), with the horizontal line indicating the median. Whiskers extend to show the rest of the distribution, except for points that are determined to be "outliers".
D) Correlation between the number of spines and dendritic length (Pearson correlation coefficient, r):Left: Correlation calculated across the entire neuron as indicated bu the shape of the neuron with apical dendrites in red and basal dendrites in blue. Center (Red): Correlation calculated only for apical dendrites . Right (Blue): Correlation calculated only for basal dendrites.
E) Dendritic branches categorized by branching order (or degree). First Degree: Dendrites originate directly from the soma. Second Degree: Dendrites branching from first-degree dendrites. Third Degree: Dendrites branching from second-degree dendrites. Color Code: Purple represents first-degree branches, transitioning to yellow for third-degree branches, showing the hierarchical organization of the dendritic tree.
F) Left Plot: Number of spines within each branch degree normalized by the total dendritic length of that degree. Significant differences observed among dendrites ((n = 21 from 7 neurons, Kruskal-Wallis test: F(2, 18) = 6.108, p = 0.04718), followed by post-hoc Dunn's test, p-value of the pairwise comparison are corrected with Bonferroni correction and are shown in the plot).
Center Plot: Spine density calculated only for branches within the apical compartment (n=7 neurons, up to 3 branch degrees). Differences found among branch degrees (n = 21 from 7 neurons, Kruskal-Wallis test: F(2, 18) = 8.289, p = 0.01585 followed by post-hoc Dunn's test, p-value of the pairwise comparison are corrected with Bonferroni correction and are shown in the plot).
Right: Spine density calculated only for branches within the basal compartment (n=7 neurons). Since 3th degree was not enough represented we conducted pairwise comparison between 1st and 2nd degree branches. No differences were found (p = 0.44, t-test)

Spatial Distribution and Activation Patterns of Calcium Events in Dendritic Spines Following BLA and CA3 Stimulation

To detect calcium signals we studied the Fluo-5F signal within each identified spine mask. Given the high number of traces recorded in each neuron and their relatively low signal-to-noise ratio we decided also in this case to develop a calcium events automatized detection strategy. We trained a neural network to identify signals that occur immediately after the optogenetic or the electrical stimulation of BLA terminals or CA3 fibers, respectively. Thus, we sorted stimulus-triggered signal (Fig. 4A) from the noise and associated each of them with their relative position on the dendritic tree. We generated a detailed map showing the positions of detected calcium transients that occurred immediately after BLA-terminal or SC stimulation (Fig. 4B). Interestingly, activation probabilities varied among spines, with individual spines displaying calcium transients at rates from 20% (once out of five sessions) to 100%. Among spines classified as “activated”, we observed that the majority of calcium transients occur in only 1 out of 5 trials (91.2% ± 4.8% of spines for BLA and 84.9% ± 4.1% for CA3), which is consistent with synaptic inputs characterized by low release probability in our experimental setup. Additionally, we observed none to very low levels of spontaneous calcium events in our traces across all trials, making it unlikely that stochastic spontaneous activity occurred precisely during the two-photon scanning period.

To further validate our classifications, we conducted two tests to ensure that spontaneous calcium events occurring during the scanning period, but unrelated to stimulation, were not misclassified as “events.” First, we identified a spontaneous calcium event occurring far from the stimulation period, which was correctly classified as a “no-event” by the classifier. When we artificially shifted the trace so that the spontaneous transient coincided with the stimulation period, the classifier reclassified it as an “event.” Second, we took a calcium event originally classified as an “event” and shifted it 1 second before or after the stimulation period. In both cases, the classifier reclassified it as a “no-event” (Fig. S1).

These results confirm that the calcium transients classified as “events” are indeed tightly linked to the stimulation period, supporting the conclusion that the synaptic inputs in our system are characterized by low release probability.

With our signal-detector model, we found that optogenetically stimulated BLA projections and electrically stimulated SCs activated a similar proportion of dendritic spines within ventral CA1 pyramidal neurons, with approximately 5% of identified spines responding to stimulation and no significant difference in activation rates between the two input sources (Fig. 4C). Furthermore, we observed that BLA-activated spines were evenly distributed across apical and basal dendrites, while CA3-activated spines showed a preference for apical dendritic compartments (Fig. 4D). To further explore the spatial organization of BLA and SCs inputs in the entire dendritic tree, we first separately analyzed the dendritic localization of BLA- or CA3-activated spines. The activated spines in response to BLA or CA3 stimulation did not exhibit a preference for any specific dendritic branch degree (Fig. 4D). Then, we compared the effects of compartment (apical vs. basal) and branch degree (first, second, third, and fourth) on the percentage of activated spines. Interestingly, spines activated by the stimulation of BLA terminals were compartment dependent as they were denser in the apical with respect to the basal dendrites ($p = 0.0037$). In contrast, the percentage of activated spines was not significantly different in branches of different degrees ($p = 0.28$).

Interestingly, a significant interaction effect was observed between compartment and branch degree ($p = 0.014$), indicating that the effect of branch degree on spine activation percentage depended on the compartment type (Fig. 4E, left panel). Multiple comparisons across branch degrees in different compartments revealed that the optogenetic stimulation of BLA terminals activated a higher percentage of spines in third degree branches of the apical compartment compared to the same branch degree in the basal compartment. A similar analysis was conducted for the percentage of activated spines in response to CA3 stimulation, revealing a consistent number of activated spines across branches, yet with a significant difference between apical and basal compartments ($p = 0.007$; Fig. 4E, right panel). Notably, while a difference in activated spines between the compartments (apical

vs. basal) is present, percentage of activated spines do not differ among branch degrees. This suggests that the influence of compartment on spine activation remains consistent across all branch degrees, and that branches are equally innervated across degrees, regardless of compartment type. We next compared the innervation between BLA and CA3 inputs. By first focusing on the apical compartment (Fig. 4F, left), we found no significant differences in the percentage of activated spines between the two input types (BLA vs. CA3) across branch degrees. Similarly, when examining the basal compartment (Fig. 4F, right), no differences were observed between BLA and CA3 innervation across branch degrees. This suggests that the distribution of activated spines in both compartments is uniform regardless of the input source or the branch degree, indicating no preferential targeting by either input type within the structural hierarchy of dendritic branches.

Based on our results, we concluded that under our experimental conditions, dendritic spines exhibiting calcium events in response to BLA stimulation were distributed broadly across the dendritic tree, lacking a clear macroscale organization. However, specific dendritic substructures, such as third-degree apical branches, may serve as preferential sites for convergence of these inputs, potentially supporting compartmentalized integration within CA1 pyramidal neurons.

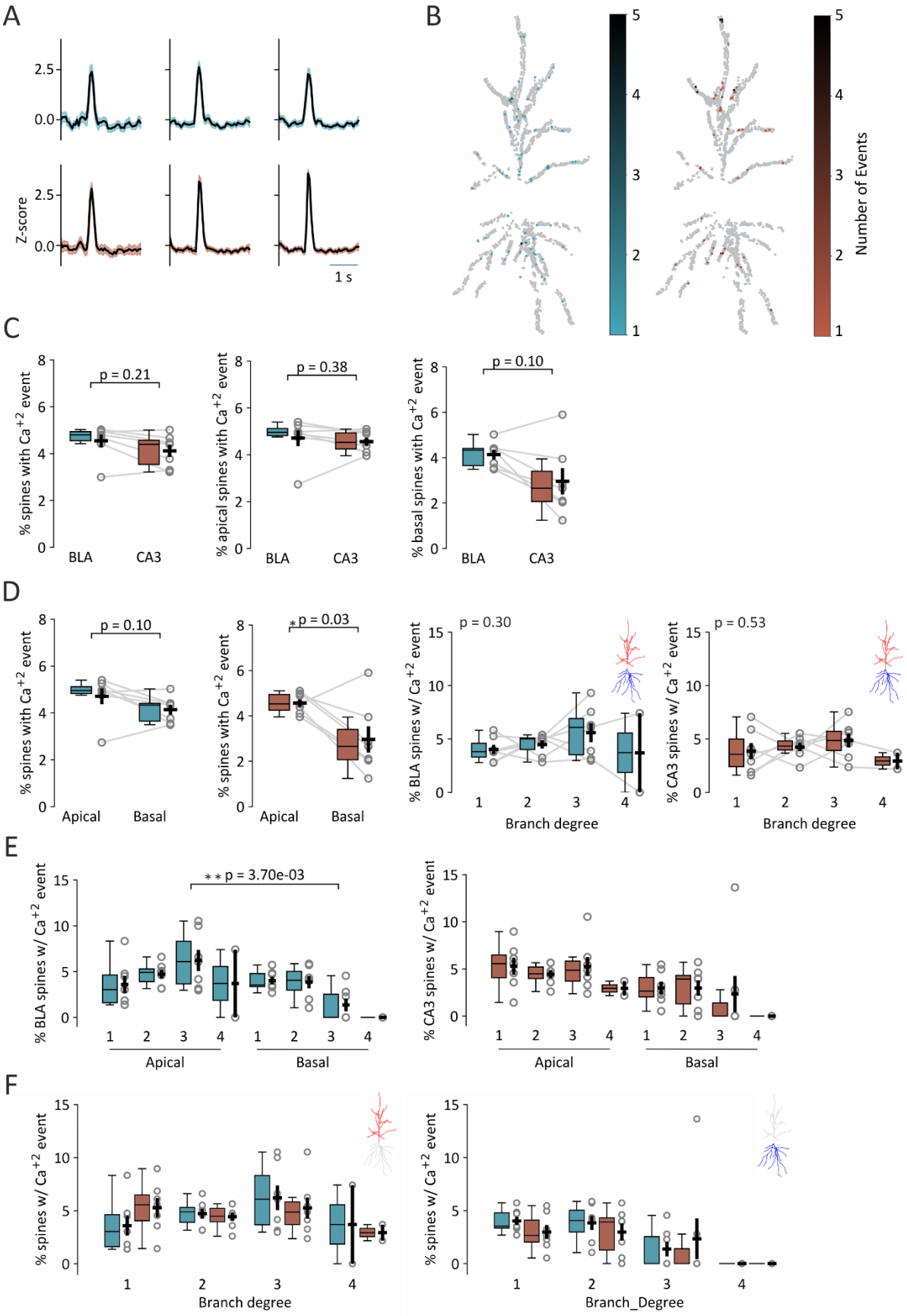
A
2.5
0.0
Z-score
2.5
0.0
1 s
B
Number of Events
C
% spines with Ca+2 event
p = 0.21
BLA
CA3
% apical spines with Ca+2 event
p = 0.38
% basal spines with Ca+2 event
p = 0.10
D
% spines with Ca+2 event
p = 0.10
Apical
Basal
*p = 0.03
% BLA spines w/ Ca+2 event
p = 0.30
Branch degree
% CA3 spines w/ Ca+2 event
p = 0.53
E
% BLA spines w/ Ca+2 event
**p = 3.70e-03
Apical
Basal
% CA3 spines w/ Ca+2 event
F
% spines w/ Ca+2 event
Branch degree
Branch_Degree

Figure 3.4. Calcium detected signals from BLA and CA3 on dendritic arborization

A) Each row represents the mean of the Z-score of the traces that were above the 99th percentile of the probability distribution generated by the model as calcium signal induced by optogenetic activation (BLA terminals, in blue) or by electric stimulation (CA3, in brown). Each column is a neuron, and the shaded area represents the 95% of the confident interval.

B) The map displays all spines identified along the dendritic tree, with those detected by the DeepD3 model shown in light grey. The left panel highlights spines activated by optogenetic stimulation of BLA inputs, marked in blue, while the right panel shows spines activated by electrical stimulation of Schaffer collaterals (SCs), marked in brown. The intensity of each dot represents the likelihood of a calcium event occurring across five trials, as indicated by the gradient bars: lighter dots signify a lower probability, and darker dots indicate a higher probability of calcium events.

C) the first graph on the left shows the percentage of the spines in which a calcium signal is detected over the total number of segmented spines. Percentage of optogenetic activated spines (BLA, in blue) and electric activated spines (CA3, in brown) do not show differences (n=7, Mann-Whitney U test). In the middle the graph shows only the percentage of the calcium events in the apical compartment. BLA vs CA3 did not show differences (n=7, Mann-Whitney U test) on the right, only the basal compartment was taken in consideration. No differences between BLA and CA are shown (n=7, T-test).

D) From the left to the right: (1) Comparison between the mean of % BLA activated spines in apical segment vs basal segment (n=7,). (2) Comparison between the mean of % CA3 activated spines in apical segment vs basal segment (n=7,). (3) Group comparison of % of BLA activated spines among branch degrees (n = 21, Kruskal-Wallis' test: F(2, 18) = 2.427, p = 0.30). (4) Group comparison of % of CA3 activated spines among branch degrees (n = 21, RM one-way ANOVA: F(2, 18) = 0.664, p = 0.52710).

E) On the left, multiple comparison of % of activated spines by BLA stimulation between apical and basal compartments among branch degrees (n=7 neurons, Two Way ANOVA followed by Tukey's HSD. Branch degree effect not significant (df=3, F= 1.31, p-value = 0.28). Compartment effect was significant (df=1, F=9.11, p-value = 0.0045). Interaction effect was significant (df = 3, F= 0.14, p-value = 0.014). Tukey's multiple comparison showed difference in the comparison between third degree apical and third degree basal (p-value = 0.0037)

On the right, multiple comparison of % of activated spines by CA3 stimulation between apical and basal compartments among branch degrees (n=7, Two Way ANOVA). Branch degree effect was not significant (df=3, F= 1, p-value = 0.40). compartment effect presented significant differences (df = 1, F= 8, p-value = 0.007). interaction effect showed no difference (df = , F = 0.18, p-value = 0.90).

F) Left panel indicates the comparison between branches degree and the input type in the apical compartment (BLA and CA3, n=7, Two Way ANOVA). The main effect of input type is not significant (n = 46, df = 1.0, F= 0.010, p-value = 0.92). The effect of the Branch degree is not significant (n = 46, df, 3, F=1.37, p-value = 0.27). The interaction effect is not significant (n=46, df=3, F=0.81, p-value = 0.49). Right panel indicates the comparison between branches degree and the input type in the basal compartment (BLA and CA3, n=7 neurons, Two Way ANOVA). The main effect of input type is not significant (n = 46, df = 1.0, F= 0.015, p-value = 0.70). The effect of the Branch degree is close to the threshold for significance (n = 46, df, 3, F=2.82, p-value = 0.51). The interaction effect is not significant (n=46, df=3, F=0.46, p-value = 0.71).

Box Plot Details: The black cross represents the mean ± SEM. The box spans the interquartile range (IQR), with the horizontal line indicating the median. Whiskers extend to show the rest of the distribution, except for points that are determined to be "outliers".

Branch-Specific Variability Shapes Synaptic Input Distribution

We finally analyzed the distribution of synaptic inputs across individual dendritic branches, hypothesizing a non-uniform distribution of BLA and CA3 inputs leading to a branch-specific dominance of these two inputs. To test this hypothesis, we examined branch-to-branch variability within individual neurons to determine whether synaptic inputs displayed significant deviation from an expected random distribution and to evaluate whether specific branches preferentially received input from BLA or CA3 inputs. To this end, we modeled the activation of spines as a binomial process, assuming a uniform activation probability across all spines of the neuron. Based on this assumption, we compared the observed number of activated spines on each branch to the expected binomial distribution for the same branch size. For each branch, we calculated the probability of obtaining the observed activated spines under the null hypothesis. Branches with p-values below a significance threshold ($p<0.05$) were considered to exhibit input patterns deviating from a random distribution. Our findings revealed that specific dendritic branches exhibited significant deviations from the neuron-wide activation pattern for both CA3 and BLA inputs (Fig. 5) suggesting that synaptic inputs might be not uniformly distributed across all dendritic branches (Fig. 5 B & C). Notably, we observed that some branches exhibited a clear bias toward one of the two inputs, with a higher-than-expected number of activated spines in response to one input type (e.g., BLA or CA3) and, at the same time, a lower number of activated spines for the other input (Fig. 5D). This pattern supports the hypothesis of input-specific specialization, where certain dendritic branches preferentially process BLA or CA3 inputs, potentially contributing to the computational specialization of individual neurons.

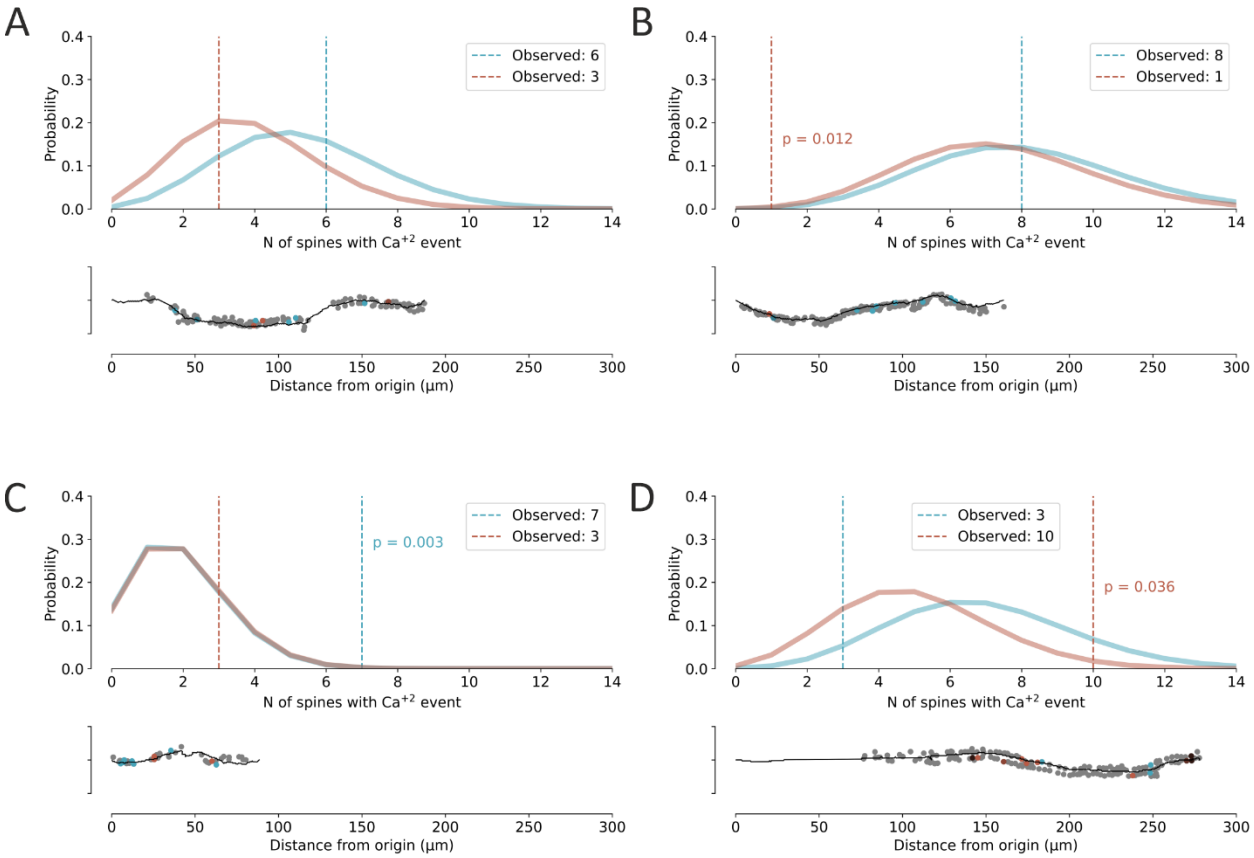

Figure 3.5 Synaptic inputs are unevenly distributed across dendritic branches
A) Branch-specific distribution of active spines (BLA in blue, CA3 in orange). Top: The observed number of active spines for BLA and CA3 on each branch aligns with the expected distribution based on a binomial probability model. The curves represent the binomial probability distribution of expected active spines for each branch, given the total number of segmented spines on that dendrite. Bottom: representation of the dendrite with in black the backbone of the dendrite, in gray the segmented spines, in blue the spines activated by BLA terminals stimulation, in orange the spines activated by Schaffer collaterals stimulation. This example shows that the observed distribution of BLA- and CA3-activated spines aligns with the expected values predicted by the binomial probability model. B In this case, the observed number of BLA-activated spines matches the expected value, while the number of CA3-activated spines is lower than the expected value. C) Here, the number of CA3-activated spines aligns with the expected value, whereas the observed number of BLA-activated spines is statistically higher than the expected value. D) This branch illustrates an extreme case where the observed CA3-activated spines exceed the binomially expected value, while the BLA-activated spines tend to be statistically lower than the expected value.

4. Discussion

In this study, we investigated the organization of functional inputs across a large portion of the dendritic tree in vCA1 PNs.

The mapping of the entire neuronal dendritic tree provided the opportunity to observe different levels of synaptic dendritic functional organizations. These include cell-to-cell variability, reflecting differences in the overall synapses number and density among individual neurons; branch-to-branch variability within a single neuron, where distinct dendritic branches differ in their synaptic input patterns; and in-branch variability, capturing the heterogeneity of synaptic connection within a single branch. These hierarchical layers of spatially organized inputs provide a framework to investigate the structure of the macro- and micro-connectivity between neurons. We focused on inputs converging on the apical and basal dendrites of vCA1 PNs from BLA and CA3, two regions strongly innervating the ventral hippocampus. The investigation of the spatial organization of functional inputs across an entire neuronal tree is challenging with conventional methodology based on 2P scanning microscopy. For this reason, we developed a comprehensive mapping approach by segmenting the dendritic tree into multiple ROIs across different z-layers. We subdivided neurons into ~ 45 z-planes and ~230 ROIs of different dimensions. Then, by using a machine learning approach, we automatically identified spines and extracted their spatial locations. This enabled us to identify approximately 1,300 spines per neuron, covering both apical and basal dendritic compartments, up to 4th degree dendrites. Using optogenetics and electric extracellular stimulation to induce BLA terminals and SCs depolarization, respectively, we imaged calcium transients in spines using two-photon calcium imaging, providing detailed insights into the functional characteristics of dendritic spines. Before analyzing single-spine calcium transients, we first assessed the distribution of automatically detected spines across the dendritic tree. We found a moderate positive correlation between dendritic length and spine number. This correlation may be partially affected by gaps in dendritic scanning.

During extended recording sessions, natural shifts in the brain slice caused dendrites to move slightly along the XYZ axes, occasionally leading some pre-defined ROIs to drift out of focus. Consequently, the DeepD3 model may have failed to detect spines within these out-of-focus ROIs, impacting the accuracy of spine counts and contributing to the reduced strength of the observed correlation. Our analysis revealed that apical dendritic compartments were more represented, both in terms of the absolute number of spines and spine density (calculated as the number of spines per unit length of dendrite). We further investigated whether spine density varied across individual branches. We observed that second-degree dendrites exhibited higher spine density compared to first-degree dendrites. However, when analyzing specific compartments, we found no significant differences in spine density across basal dendrites. In contrast, within the apical compartment, third-degree dendrites displayed greater spine density than first-degree dendrites of the same compartment. The latter observation might likely be due to the already reported sparser spine density on the proximal apical trunk of CA1 PNs (Megias et al., 2001). Since we observed that spine density varied across branches, we decided to quantify spines activation as the percentage of spines that presented a calcium event relative to the number of segmented spines. With the use of a customized neural network, we identified calcium transients, and we found that optogenetic stimulation of BLA terminals activated about 5% of all imaged spines in the postsynaptic neuron, a proportion similar with respect to that activated by Schaffer collaterals electrical stimulation. Interestingly, the spines activated by CA3 stimulation exhibited greater variability between neurons, as indicated by a broader interquartile range (IQR) compared to the activation percentages observed with BLA stimulation. This variability could be attributed to the highly variable number of synapses that CA3 forms on CA1 neurons (Druckmann *et al.*, 2014). However, we cannot exclude the possibility that such wider IQR distribution could be influenced by the stimulation method. The positioning of the stimulation pipette, indeed, may have contributed to this variability, as slight differences in its placement could have stimulated distinct subsets of Schaffer collaterals bundles. Due to the approach we used, it is difficult to directly compare our results with previous findings. For example, while Druckmann et al. (2014) used mGRASP to

anatomically map CA3 inputs and reported a synaptic density higher than our observed proportion of activated spines, our imaging approach might underestimate the number of synapses for several reasons. First, the use of acute slices likely leads to the loss of fibers that are cut during slicing, reducing the number of potential stimulated connections. Second, we only map synapses that are active during stimulation, leaving inactive connections unaccounted for. Third, small synapses or synapses with thin necks may be difficult to detect with our resolution due to minimal calcium fluctuations or limited diffusion of Fluo-5 and Alexa Fluor into the spine head. These small or inactive synapses are more effectively captured using mGRASP, which does not rely on calcium activity for detection.

However, while mGRASP provides an elegant way of mapping synapses with high anatomical resolution, it also does not fit for our purpose. In particular, mGRASP cannot assess synaptic activity or the functional state of identified synapses, which are crucial for understanding synaptic integration in the postsynaptic neuron. Since our future goal is to investigate how signals from neighboring active synapses originating from different input sources are integrated, our approach offers unique advantages. By selectively activating synapses and simultaneously recording the postsynaptic cell's electrical output, we can dynamically study how active inputs are integrated and how dendritic and somatic compartments contribute to this process. This functional readout is essential to address questions about the computational properties of neurons, such as how synaptic inputs interact to produce sublinear or supralinear integration. Moreover, the ability to manipulate active synapses with temporal precision allows us to probe the interplay between different inputs under physiological and experimental conditions, a level of functional understanding not achievable with purely anatomical methods such as mGRASP.

We examined the distribution of spines that showed calcium events across the dendritic tree. Our findings revealed that spines activated by CA3 inputs were predominantly located on apical dendrites, whereas those activated by BLA inputs were more evenly distributed between apical and basal compartments. Despite these differences in distribution, the density of activated spines did not significantly differ between CA3 and BLA inputs within either compartment. Although the density of BLA-activated spines did not differ across

compartments, third-degree branches in the apical segment exhibited a higher density of active spines compared to their counterparts in the basal compartment. This result is particularly intriguing as it suggests that BLA inputs preferentially target third-degree apical dendrites. Such a pattern hints at the possibility that specific dendritic branches may receive denser innervation than others, potentially indicating a functional specialization of these branches in integrating BLA-driven signals. By examining the branch-to-branch variability of synaptic inputs, we found that active spines on certain branches deviated significantly from the expected random distribution. Notably, some branches displayed a non-random preference for BLA inputs, while others exhibited a similar preference for CA3 inputs.

The non-uniform targeting of BLA and CA3 inputs suggests that dendrites may encode distinct aspects of incoming information. BLA inputs to the CA1 region, for example, have been shown to convey information about the emotional valence of stimuli, such as positive or negative associations with specific contexts (Beyeler et al., 2016; Yang et al., 2017). Such input specificity may allow certain branches to prioritize valence-related information from the BLA while others process spatial or memory-related information from CA3 inputs (Lovett-Barron et al., 2014). This functional specialization of branches could reflect a broader organizational principle of CA1 neurons, wherein certain branches act as hubs for specific types of input, potentially influencing the neuron's firing output, while others subserve integrative or modulatory roles. We can speculate that the presence of differently innervated branches within a single neuron could enable the neuron to independently respond to specific input patterns either from BLA or CA3. This might also support signal multiplexing where two distinct different firing patterns determined, for instance, by the activation of BLA, or a combination of CA3 and BLA can be independently transmitted through the same neuronal pathway (Naud & Sprekeler, 2018). Such multiplexing may enhance the encoding capacity of CA1 neurons, allowing for the disambiguation of similar stimuli and sensory representations.

Limitations of the study

Although our experimental and methodological approach aimed to minimize potential confounding factors, certain aspects may still have influenced parts of the data and its interpretation.

First, we used electrical stimulation to activate CA3 SCs and optogenetics to activate BLA terminals in vCA1. It might be argued that the use of two different stimulation methods could lead to difference in stimulation intensity thus potentially accounting for differences in the percentage of activated BLA or CA3 spines. However, in our experimental conditions it was not possible to stimulate both input sources either optogenetically or electrically. Indeed, the stereotaxic injection of a virus into CA3 to express opsins would have resulted in a contamination of expression in the CA1 hippocampal region. Although the connections within CA1 neurons are minimal (Deuchars and Thomson, 1996), rhodopsin expression in these neurons would cause direct depolarization of the patched cell, making it impossible to accurately record calcium entry in individual spines. On the other hand, while Schaffer collaterals are remarkably spatially organized in a defined bundle, to our knowledge, BLA fibers are more sparsely organized. For this reason, we couldn't selectively activate BLA axons using an electric stimulator.

Second, while scanning z-layers, some parts of the ROIs may have been out of focus, potentially resulting in certain portions of dendrites not being fully represented in our neurons. The presence of these "gaps" could potentially prevent the identification of specific synaptic spatial arrangements. While this remains an issue to be addressed, we believe that by increasing the sample number we could still identify spatial synaptic motifs in sub-regions not affected by gaps.

Future perspectives

In this study, we focused on mapping functional glutamatergic inputs, specifically CA3 and BLA projections onto vCA1 PNs. However, it is crucial to determine whether inputs from the BLA contacting CA1 follow a specific connectivity pattern. Insights into the connectivity patterns between CA3 and CA1 have been provided by Druckmann et al., 2014, but to date, similar information is lacking for BLA-to-CA1 fibers. For this reason, in our future work we will better elucidate how BLA terminals are organized on vCA1 pyramidal neurons performing anatomical studies using, for instance, the GRASP technique (Feinberg et al., 2008). Moreover, as above, scattered, projection-defined neuronal populations within BLA selectively activate during encoding and retrieval of memories associated with either positive or negative valence. Interestingly, BLA neurons projecting to the vCA1 respond to both positive and negative predicting cues with no marked bias, suggesting that, within the whole responding population, two distinct subnetworks relay opposite information to vCA1. To explore this, we aim to use Fos-TRAP2 mice in behavioral conditioning paradigms, to selectively express ChR in the amygdala populations responsive to negative or positive valence. We will inject cre-dependent ChR (AAV-DIO-ChR2) in the BLA and subject separate groups of mice to either fear or reward conditioning. Fear conditioning will involve pairing a neutral stimulus, such as a tone, with an aversive stimulus (an electric shock). Reward conditioning will be implemented by keeping the mice in a state of mild food deprivation and training them to associate the presentation of a tone with access to sugar water until the association is formed. On the day of memory retrieval, tamoxifen will be administered, and the tone will be presented to activate the Fos gene in engram cells. The tamoxifen will bind to the modified estrogen receptor fused to the CRE protein (CRE/ER), enabling its relocation to the nucleus. This process will drive the expression of the CRE-dependent ChR, ensuring that rhodopsin is expressed exclusively in the cells activated during memory retrieval. After three weeks, using the experimental approach described in this thesis, we will investigate whether BLA functional inputs are differentially organized onto CA1 pyramidal neurons according to valence-specific activation.

Supplementary Figures

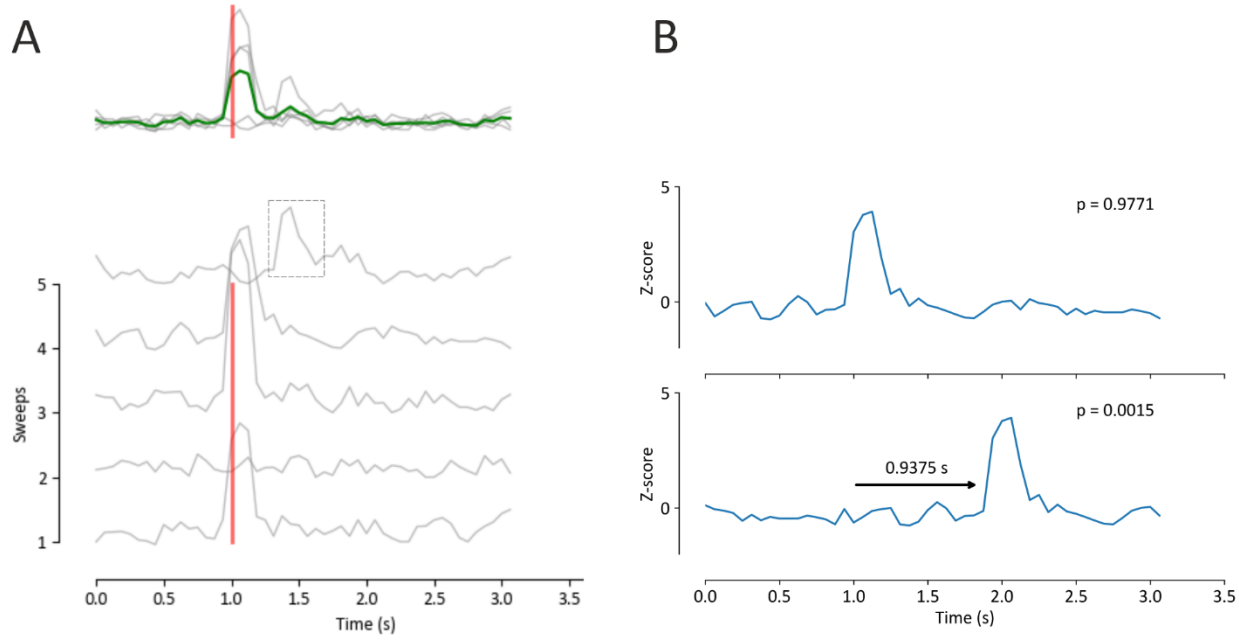

Figure S1. Event detection control
A. Representative traces of five trials in an individual spine. Top: Calcium average trace of 5 sweeps is shown in green, with the vertical red line indicating the time of stimulation. Bottom: Individual calcium traces from the 5 sweeps are displayed in gray. In the example, three out of five sweeps exhibit a calcium transient aligned with the stimulation (1, 3 and 4), while the fifth sweep shows a spontaneous calcium transient occurring away from the stimulation (dashed box). **B.** Example calcium trace used as a control to test the timing sensitivity of the classifier. Top: The original trace from the fourth sweep in panel A, classified as an "event" with 97% probability. Bottom: The same trace shifted 0.9375 seconds (15 sampling points) to the right is labeled as an "event" with only a probability of 0.015%.

Bibliography

Abrahamsson, T. *et al.* (2012) 'Thin Dendrites of Cerebellar Interneurons Confer Sublinear Synaptic Integration and a Gradient of Short-Term Plasticity', *Neuron*, 73(6). doi: 10.1016/j.neuron.2012.01.027.

Adhikari, A. *et al.* (2015) 'Basomedial amygdala mediates top-down control of anxiety and fear', *Nature*, 527(7577). doi: 10.1038/nature15698.

Alheid, G. F. (2003) 'Extended amygdala and basal forebrain', in *Annals of the New York Academy of Sciences*. doi: 10.1111/j.1749-6632.2003.tb07082.x.

Alsubaie, R. *et al.* (2021) 'Control of parallel hippocampal output pathways by amygdalar long-range inhibition.', *eLife*, 10, pp. 1–29. doi: 10.7554/eLife.74758.

Ambroggi, F. *et al.* (2008) 'Basolateral Amygdala Neurons Facilitate Reward-Seeking Behavior by Exciting Nucleus Accumbens Neurons', *Neuron*, 59(4). doi: 10.1016/j.neuron.2008.07.004.

Andersen, P., Bliss, T. V. P. and Skrede, K. K. (1971) 'Lamellar organization of hippocampal excitatory pathways', *Experimental Brain Research*, 13(2). doi: 10.1007/BF00234087.

Bannerman, D. M. *et al.* (2003) 'Ventral hippocampal lesions affect anxiety but not spatial learning', *Behavioural Brain Research*, 139(1–2). doi: 10.1016/S0166-4328(02)00268-1.

Bannerman, D. M. *et al.* (2004) 'Regional dissociations within the hippocampus - Memory and anxiety', *Neuroscience and Biobehavioral Reviews*. doi: 10.1016/j.neubiorev.2004.03.004.

Beyeler, A. *et al.* (2016) 'Divergent Routing of Positive and Negative Information from the Amygdala during Memory Retrieval', *Neuron*, 90(2), pp. 348–361. doi: 10.1016/j.neuron.2016.03.004.

Beyeler, A. *et al.* (2018) 'Organization of Valence-Encoding and Projection-Defined Neurons in the Basolateral Amygdala', *Cell Reports*, 22(4), pp. 905–918. doi: 10.1016/j.celrep.2017.12.097.

Boyden, E. S. *et al.* (2005) 'Millisecond-timescale, genetically targeted optical control of neural activity', *Nature Neuroscience*, 8(9). doi: 10.1038/nn1525.

Branco, T. and Häusser, M. (2011) 'Synaptic Integration Gradients in Single Cortical Pyramidal Cell Dendrites', *Neuron*, 69(5). doi: 10.1016/j.neuron.2011.02.006.

Burgos-Robles, A. *et al.* (2017) 'Amygdala inputs to prefrontal cortex guide behavior amid conflicting cues of reward and punishment', *Nature Neuroscience*, 20(6). doi: 10.1038/nn.4553.

Cadogan, A. K. *et al.* (1994) 'Social interaction increases 5-HT release and cAMP efflux in the rat ventral hippocampus in vivo', *Behavioural Pharmacology*, 5(3). doi: 10.1097/00008877-199406000-00007.

Carlezon, W. A. and Thomas, M. J. (2009) 'Biological substrates of reward and aversion: A nucleus accumbens activity hypothesis', *Neuropharmacology*. doi: 10.1016/j.neuropharm.2008.06.075.

Cembrowski, M. S. *et al.* (2016) 'Spatial Gene-Expression Gradients Underlie Prominent Heterogeneity of CA1 Pyramidal Neurons', *Neuron*, 89(2). doi: 10.1016/j.neuron.2015.12.013.

Chater, T. E. and Goda, Y. (2021) 'My Neighbour Hetero — deconstructing the mechanisms underlying heterosynaptic plasticity', *Current Opinion in Neurobiology*. doi: 10.1016/j.conb.2020.10.007.

Chen, X. *et al.* (2011) 'Functional mapping of single spines in cortical neurons in vivo', *Nature*, 475(7357), pp. 501–505. doi: 10.1038/nature10193.

Chiovini, B. *et al.* (2014) 'Dendritic Spikes Induce Ripples in Parvalbumin Interneurons during Hippocampal

Sharp Waves', *Neuron*, 82(4). doi: 10.1016/j.neuron.2014.04.004.

Ciocchi, S. *et al.* (2015) 'Selective information routing by ventral hippocampal CA1 projection neurons', *Science*, 348(6234). doi: 10.1126/science.aaa3245.

Cruikshank, S. J. *et al.* (2010) 'Pathway-Specific Feedforward Circuits between Thalamus and Neocortex Revealed by Selective Optical Stimulation of Axons', *Neuron*, 65(2). doi: 10.1016/j.neuron.2009.12.025.

Davidson, B. L. and Breakefield, X. O. (2003) 'Viral vectors for gene delivery to the nervous system', *Nature Reviews Neuroscience*, 4(5). doi: 10.1038/nrn1104.

Davidson, R. J. (2002) 'Anxiety and affective style: Role of prefrontal cortex and amygdala', *Biological Psychiatry*. doi: 10.1016/S0006-3223(01)01328-2.

Diehl, G. W. *et al.* (2017) 'Grid and Nongrid Cells in Medial Entorhinal Cortex Represent Spatial Location and Environmental Features with Complementary Coding Schemes', *Neuron*, 94(1). doi: 10.1016/j.neuron.2017.03.004.

Druckmann, S. *et al.* (2014) 'Structured Synaptic Connectivity between Hippocampal Regions', *Neuron*, 81(3), pp. 629–640. doi: 10.1016/j.neuron.2013.11.026.

Eilers, J. and Konnerth, A. (2009) 'Dye loading with patch pipettes', *Cold Spring Harbor Protocols*, 4(4). doi: 10.1101/pdb.prot5201.

Etkin, A., Egner, T. and Kalisch, R. (2011) 'Emotional processing in anterior cingulate and medial prefrontal cortex', *Trends in Cognitive Sciences*. doi: 10.1016/j.tics.2010.11.004.

Everitt, B. J. *et al.* (1991) 'The basolateral amygdala-ventral striatal system and conditioned place preference: Further evidence of limbic-striatal interactions underlying reward-related processes', *Neuroscience*, 42(1). doi: 10.1016/0306-4522(91)90145-E.

Fanselow, M. S. and Dong, H.-W. (2010) 'Are the dorsal and ventral hippocampus functionally distinct structures?', *Neuron*, 65(1), pp. 7–19. doi: 10.1016/j.neuron.2009.11.031.

Fanselow, M. S. and LeDoux, J. E. (1999) 'Why we think plasticity underlying pavlovian fear conditioning occurs in the basolateral amygdala', *Neuron*. doi: 10.1016/S0896-6273(00)80775-8.

Felix-Ortiz, A. C. *et al.* (2013) 'BLA to vHPC inputs modulate anxiety-related behaviors', *Neuron*, 79(4), pp. 658–664. doi: 10.1016/j.neuron.2013.06.016.

Felix-Ortiz, A. C. and Tye, K. M. (2014) 'Amygdala inputs to the ventral hippocampus bidirectionally modulate social behavior', *Journal of Neuroscience*, 34(2). doi: 10.1523/JNEUROSCI.4257-13.2014.

Fernholz, M. H. P. *et al.* (2024) 'DeepD3, an open framework for automated quantification of dendritic spines', *PLoS Computational Biology*, 20(2). doi: 10.1371/journal.pcbi.1011774.

Frank, A. C. *et al.* (2018) 'Hotspots of dendritic spine turnover facilitate clustered spine addition and learning and memory', *Nature Communications*, 9(1). doi: 10.1038/s41467-017-02751-2.

Frijda, N. H. (2017) *The laws of emotion*, *The Laws of Emotion*. doi: 10.4324/9781315086071.

Gergues, M. M. *et al.* (2020) 'Circuit and molecular architecture of a ventral hippocampal network', *Nature Neuroscience*, 23(11), pp. 1444–1452. doi: 10.1038/s41593-020-0705-8.

Goosens, K. A. and Maren, S. (2001) 'Contextual and auditory fear conditioning are mediated by the lateral, basal, and central amygdaloid nuclei in rats', *Learning and Memory*, 8(3). doi: 10.1101/lm.37601.

Graham, J. *et al.* (2021) 'High-Frequency Stimulation of Ventral CA1 Neurons Reduces Amygdala Activity and Inhibits Fear', *Frontiers in Behavioral Neuroscience*, 15(March), pp. 1–13. doi: 10.3389/fnbeh.2021.595049.

Grynkiewicz, G., Poenie, M. and Tsien, R. Y. (1985) 'A new generation of Ca2+ indicators with greatly improved fluorescence properties', *Journal of Biological Chemistry*. doi: 10.1016/s0021-9258(19)83641-4.

Hamada, S. *et al.* (2021) 'An engineered channelrhodopsin optimized for axon terminal activation and circuit mapping', *Communications Biology*, 4(1). doi: 10.1038/s42003-021-01977-7.

Harvey, C. D. and Svoboda, K. (2007) 'Locally dynamic synaptic learning rules in pyramidal neuron dendrites', *Nature*, 450(7173), pp. 1195–1200. doi: 10.1038/nature06416.

Herman, J. P. and Cullinan, W. E. (1997) 'Neurocircuitry of stress: Central control of the hypothalamo-pituitary-adrenocortical axis', *Trends in Neurosciences*, 20(2). doi: 10.1016/S0166-2236(96)10069-2.

Higley, M. J. and Sabatini, B. L. (2012) 'Calcium signaling in dendritic spines', *Cold Spring Harbor Perspectives in Biology*, 4(4). doi: 10.1101/cshperspect.a005686.

Huang, W. C. *et al.* (2020) 'Social Behavior Is Modulated by Valence-Encoding mPFC-Amygdala Sub-circuitry', *Cell Reports*, 32(2). doi: 10.1016/j.celrep.2020.107899.

Iacaruso, M. F., Gasler, I. T. and Hofer, S. B. (2017) 'Synaptic organization of visual space in primary visual cortex', *Nature*, 547(7664). doi: 10.1038/nature23019.

Ishikawa, T. *et al.* (2020) 'Functional Multiple-Spine Calcium Imaging from Brain Slices', *STAR Protocols*, 1(3). doi: 10.1016/j.xpro.2020.100121.

Jadi, M. *et al.* (2012) 'Location-dependent effects of inhibition on local spiking in pyramidal neuron dendrites', *PLoS Computational Biology*, 8(6). doi: 10.1371/journal.pcbi.1002550.

Jay, T. M. and Witter, M. P. (1991) 'Distribution of hippocampal CA1 and subicular efferents in the prefrontal cortex of the rat studied by means of anterograde transport of Phaseolus vulgaris-leucoagglutinin', *Journal of Comparative Neurology*, 313(4). doi: 10.1002/cne.903130404.

Jia, H. *et al.* (2010) 'Dendritic organization of sensory input to cortical neurons in vivo', *Nature*, 464(7293). doi: 10.1038/nature08947.

Jimenez, J. C. *et al.* (2018) 'Anxiety Cells in a Hippocampal-Hypothalamic Circuit.', *Neuron*, 97(3), pp. 670-683.e6. doi: 10.1016/j.neuron.2018.01.016.

Jimenez, J. C. *et al.* (2020) 'Contextual fear memory retrieval by correlated ensembles of ventral CA1 neurons', *Nature Communications*, 11(1). doi: 10.1038/s41467-020-17270-w.

Kantak, K. M. *et al.* (2002) 'Dissociable effects of lidocaine inactivation of the rostral and caudal basolateral amygdala on the maintenance and reinstatement of cocaine-seeking behavior in rats', *Journal of Neuroscience*, 22(3). doi: 10.1523/jneurosci.22-03-01126.2002.

Kastellakis, G. *et al.* (2015) 'Synaptic clustering within dendrites: An emerging theory of memory formation', *Progress in Neurobiology*. doi: 10.1016/j.pneurobio.2014.12.002.

Kheirbek, M. A. *et al.* (2013) 'Differential control of learning and anxiety along the dorsoventral axis of the dentate gyrus', *Neuron*, 77(5). doi: 10.1016/j.neuron.2012.12.038.

Kim, J. *et al.* (2016) 'Antagonistic negative and positive neurons of the basolateral amygdala', *Nature Neuroscience*, 19(12). doi: 10.1038/nn.4414.

Kim, J. *et al.* (2017) 'Basolateral to Central Amygdala Neural Circuits for Appetitive Behaviors', *Neuron*, 93(6). doi: 10.1016/j.neuron.2017.02.034.

Kjelstrup, K. G. *et al.* (2002) 'Reduced fear expression after lesions of the ventral hippocampus', *Proceedings of the National Academy of Sciences of the United States of America*, 99(16). doi: 10.1073/pnas.152112399.

Kleindienst, T. *et al.* (2011) 'Activity-dependent clustering of functional synaptic inputs on developing hippocampal dendrites', *Neuron*, 72(6), pp. 1012–1024. doi: 10.1016/j.neuron.2011.10.015.

Lang, P. J. (1995) 'The emotion probe: Studies of motivation and attention.', *American Psychologist*, 50(5). doi: 10.1037/0003-066x.50.5.372.

Larkum, M. (2013) 'A cellular mechanism for cortical associations: An organizing principle for the cerebral cortex', *Trends in Neurosciences*. doi: 10.1016/j.tins.2012.11.006.

Larkum, M. E. *et al.* (2009) 'Synaptic integration in tuft dendrites of layer 5 pyramidal neurons: A new unifying principle', *Science*, 325(5941). doi: 10.1126/science.1171958.

Larkum, M. E., Zhu, J. J. and Sakmann, B. (1999) 'A new cellular mechanism for coupling inputs arriving at different cortical layers', *Nature*, 398(6725). doi: 10.1038/18686.

LeDoux, J. E. (2000) 'Emotion circuits in the brain', *Annual Review of Neuroscience*. doi: 10.1146/annurev.neuro.23.1.155.

Losonczy, A. and Magee, J. C. (2006) 'Integrative Properties of Radial Oblique Dendrites in Hippocampal CA1 Pyramidal Neurons', *Neuron*, 50(2). doi: 10.1016/j.neuron.2006.03.016.

Lovett-Barron, M. *et al.* (2012) 'Regulation of neuronal input transformations by tunable dendritic inhibition', *Nature Neuroscience*, 15(3). doi: 10.1038/nn.3024.

Madisen, L. *et al.* (2012) 'A toolbox of Cre-dependent optogenetic transgenic mice for light-induced activation and silencing', *Nature Neuroscience*, 15(5). doi: 10.1038/nn.3078.

Mank, M. *et al.* (2008) 'A genetically encoded calcium indicator for chronic in vivo two-photon imaging', *Nature Methods*, 5(9). doi: 10.1038/nmeth.1243.

Margrie, T. W., Brecht, M. and Sakmann, B. (2002) 'In vivo, low-resistance, whole-cell recordings from neurons in the anaesthetized and awake mammalian brain', *Pflugers Archiv European Journal of Physiology*, 444(4). doi: 10.1007/s00424-002-0831-z.

McCulloch, W. S. and Pitts, W. (1943) 'A logical calculus of the ideas immanent in nervous activity', *The Bulletin of Mathematical Biophysics*, 5(4). doi: 10.1007/BF02478259.

Moga, M. M. *et al.* (1990) 'Organization of cortical, basal forebrain, and hypothalamic afferents to the parabrachial nucleus in the rat.', *The Journal of comparative neurology*, 295(4), pp. 624–661. doi: 10.1002/cne.902950408.

Moser, E., Moser, M. B. and Andersen, P. (1993) 'Spatial learning impairment parallels the magnitude of dorsal hippocampal lesions, but is hardly present following ventral lesions', *Journal of Neuroscience*, 13(9). doi: 10.1523/jneurosci.13-09-03916.1993.

Moser, M. B. *et al.* (1995) 'Spatial learning with a minislab in the dorsal hippocampus.', *Proceedings of the National Academy of Sciences of the United States of America*, 92(21), pp. 9697–9701. doi: 10.1073/pnas.92.21.9697.

Nagel, G. *et al.* (2005) 'Light activation of Channelrhodopsin-2 in excitable cells of caenorhabditis elegans triggers rapid behavioral responses', *Current Biology*, 15(24). doi: 10.1016/j.cub.2005.11.032.

Namburi, P. *et al.* (2015) 'A circuit mechanism for differentiating positive and negative associations', *Nature*, 520(7549). doi: 10.1038/nature14366.

Naud, R. and Sprekeler, H. (2018) 'Sparse bursts optimize information transmission in a multiplexed neural code', *Proceedings of the National Academy of Sciences of the United States of America*, 115(27). doi: 10.1073/pnas.1720995115.

Okuyama, T. *et al.* (2016) 'Ventral CA1 neurons store social memory', *Science*, 353(6307). doi: 10.1126/science.aaf7003.

Pagkalos, M., Chavlis, S. and Poirazi, P. (2023) 'Introducing the Dendrify framework for incorporating dendrites to spiking neural networks', *Nature Communications*, 14(1). doi: 10.1038/s41467-022-35747-8.

Palmer, L., Murayama, M. and Larkum, M. (2012) 'Inhibitory regulation of dendritic activity in vivo', *Frontiers in Neural Circuits*. doi: 10.3389/fncir.2012.00026.

Paton, J. J. *et al.* (2006) 'The primate amygdala represents the positive and negative value of visual stimuli during learning', *Nature*, 439(7078). doi: 10.1038/nature04490.

Pessoa, L. (2008) 'On the relationship between emotion and cognition', *Nature Reviews Neuroscience*. doi: 10.1038/nrn2317.

Petreanu, L. *et al.* (2007) 'Channelrhodopsin-2-assisted circuit mapping of long-range callosal projections', *Nature Neuroscience*, 10(5), pp. 663–668. doi: 10.1038/nn1891.

Pi, G. *et al.* (2020) 'Posterior basolateral amygdala to ventral hippocampal CA1 drives approach behaviour to exert an anxiolytic effect', *Nature Communications*, 11(1), pp. 1–15. doi: 10.1038/s41467-019-13919-3.

Pikkarainen, M. *et al.* (1999) 'Projections from the lateral, basal, and accessory basal nuclei of the amygdala to the hippocampal formation in rat', *Journal of Comparative Neurology*, 403(2). doi: 10.1002/(SICI)1096-9861(19990111)403:2<229::AID-CNE7>3.0.CO;2-P.

Pitkänen, A *et al.* (2000) 'Reciprocal connections between the amygdala and the hippocampal formation, perirhinal cortex, and postrhinal cortex in rat. A review.', *Annals of the New York Academy of Sciences*, 911, pp. 369–391. doi: 10.1111/j.1749-6632.2000.tb06738.x.

Pitkänen, Asla *et al.* (2000) 'Reciprocal connections between the amygdala and the hippocampal formation, perirhinal cortex, and postrhinal cortex in rat', *Annals of the New York Academy of Sciences*, 911, pp. 369–391. doi: 10.1111/j.1749-6632.2000.tb06738.x.

Pitkänen, A., Savander, V. and LeDoux, J. E. (1997) 'Organization of intra-amygdaloid circuitries in the rat: An emerging framework for understanding functions of the amygdala', *Trends in Neurosciences*. doi: 10.1016/S0166-2236(97)01125-9.

Poirazi, P., Brannon, T. and Mel, B. W. (2003) *Shepherd RON simulation environment (Hines and Carnevale, and Brayton*, *Neuron*.

Poirazi, P. and Mel, B. W. (2001) 'Impact of active dendrites and structural plasticity on the memory capacity of neural tissue', *Neuron*, 29(3). doi: 10.1016/S0896-6273(01)00252-5.

Polsky, A., Mel, B. W. and Schiller, J. (2004) 'Computational subunits in thin dendrites of pyramidal cells', *Nature Neuroscience*, 7(6). doi: 10.1038/nn1253.

Price, J. L. *et al.* (1987) 'Handbook of chemical neuroanatomy'.

Rah, J. C. *et al.* (2013) 'Thalamocortical input onto layer 5 pyramidal neurons measured using quantitative large-scale array tomography', *Frontiers in Neural Circuits*, 7(NOV). doi: 10.3389/fncir.2013.00177.

Reed, S. J. *et al.* (2018) 'Coordinated Reductions in Excitatory Input to the Nucleus Accumbens Underlie Food Consumption', *Neuron*, 99(6). doi: 10.1016/j.neuron.2018.07.051.

Rhodes, P. (2006) 'The properties and implications of NMDA spikes in neocortical pyramidal cells', *Journal of Neuroscience*, 26(25). doi: 10.1523/JNEUROSCI.3791-05.2006.

Rizvi, T. A. *et al.* (1991) 'Connections between the central nucleus of the amygdala and the midbrain periaqueductal gray: topography and reciprocity.', *The Journal of comparative neurology*, 303(1), pp. 121–

131. doi: 10.1002/cne.903030111.

Rogan, M. T., Staubli, U. V. and LeDoux, J. E. (1997) 'Fear conditioning induces associative long-term potentiation in the amygdala', *Nature*, 390(6660). doi: 10.1038/37601.

Rolls, E. T. (2004) 'Convergence of sensory systems in the orbitofrontal cortex in primates and brain design for emotion', in *Anatomical Record - Part A Discoveries in Molecular, Cellular, and Evolutionary Biology*. doi: 10.1002/ar.a.20126.

Roy, M., Shohamy, D. and Wager, T. D. (2012) 'Ventromedial prefrontal-subcortical systems and the generation of affective meaning', *Trends in Cognitive Sciences*. doi: 10.1016/j.tics.2012.01.005.

Russo, S. J. and Nestler, E. J. (2013) 'The brain reward circuitry in mood disorders', *Nature reviews neuroscience*, 14(9), pp. 609–625.

Sabatini, B. L., Oertner, T. G. and Svoboda, K. (2002) 'The life cycle of Ca2+ ions in dendritic spines', *Neuron*, 33(3). doi: 10.1016/S0896-6273(02)00573-1.

Sah, P. *et al.* (2003) 'The amygdaloid complex: Anatomy and physiology', *Physiological Reviews*. doi: 10.1152/physrev.00002.2003.

Sauvage, M. M., Nakamura, N. H. and Beer, Z. (2013) 'Mapping memory function in the medial temporal lobe with the immediate-early gene Arc', *Behavioural Brain Research*, 254, pp. 22–33. doi: 10.1016/j.bbr.2013.04.048.

Schoenbaum, G., Chiba, A. A. and Gallagher, M. (1998) 'Orbitofrontal cortex and basolateral amygdala encode expected outcomes during learning', *Nature Neuroscience*, 1(2). doi: 10.1038/407.

Schroeder, J. P. and Packard, M. G. (2002) 'Posttraining intra-basolateral amygdala scopolamine impairs food-and amphetamine-induced conditioned place preferences.', *Behavioral neuroscience*, 116(5), p. 922.

Schultz, C. and Engelhardt, M. (2014) 'Anatomy of the hippocampal formation', in *The Hippocampus in Clinical Neuroscience*. doi: 10.1159/000360925.

Schultz, W. (2000) 'Multiple reward signals in the brain', *Nature reviews neuroscience*, 1(3), pp. 199–207.

Shabel, S. J. and Janak, P. H. (2009) 'Substantial similarity in amygdala neuronal activity during conditioned appetitive and aversive emotional arousal', *Proceedings of the National Academy of Sciences of the United States of America*, 106(35). doi: 10.1073/pnas.0905580106.

Soares-Cunha, C. *et al.* (2020) 'Nucleus accumbens medium spiny neurons subtypes signal both reward and aversion.', *Molecular psychiatry*, 25(12), pp. 3241–3255. doi: 10.1038/s41380-019-0484-3.

Sosa, M., Joo, H. R. and Frank, L. M. (2020) 'Dorsal and Ventral Hippocampal Sharp-Wave Ripples Activate Distinct Nucleus Accumbens Networks', *Neuron*, 105(4). doi: 10.1016/j.neuron.2019.11.022.

Stuart, G. *et al.* (1997) 'Action potential initiation and backpropagation in neurons of the mammalian CNS', *Trends in Neurosciences*, 20(3). doi: 10.1016/S0166-2236(96)10075-8.

Svoboda, K., Tank, D. W. and Denk, W. (1996) 'Direct measurement of coupling between dendritic spines and shafts', *Science*, 272(5262). doi: 10.1126/science.272.5262.716.

Swanson, L. W. and Petrovich, G. D. (1998) 'What is the amygdala?', *Trends in Neurosciences*, 21(8), pp. 323–331. doi: 10.1016/S0166-2236(98)01265-X.

Takahashi, N. *et al.* (2012) 'Locally Synchronized Synaptic Inputs', *Science*, 335(6066), pp. 353–356. doi: 10.1126/science.1210362.

Tye, K. M. *et al.* (2008) 'Rapid strengthening of thalamo-amygdala synapses mediates cue-reward learning',

Nature, 453(7199). doi: 10.1038/nature06963.

Tye, K. M. *et al.* (2011) 'Amygdala circuitry mediating reversible and bidirectional control of anxiety', *Nature*, 471(7338). doi: 10.1038/nature09820.

Varga, Z. *et al.* (2011) 'Dendritic coding of multiple sensory inputs in single cortical neurons in vivo', *Proceedings of the National Academy of Sciences of the United States of America*, 108(37). doi: 10.1073/pnas.1112355108.

Wee, R. W. *et al.* (2021) 'Hippocampal ghrelin signalling informs the decision to eat', *bioRxiv*.

White, N. M. and McDonald, R. J. (1993) 'Acquisition of a spatial conditioned place preference is impaired by amygdala lesions and improved by fornix lesions', *Behavioural Brain Research*, 55(2). doi: 10.1016/0166-4328(93)90122-7.

Xiu, J. *et al.* (2014) 'Visualizing an emotional valence map in the limbic forebrain by TAI-FISH', *Nature Neuroscience*, 17(11). doi: 10.1038/nn.3813.

Yizhar, O. *et al.* (2011) 'Optogenetics in Neural Systems', *Neuron*. doi: 10.1016/j.neuron.2011.06.004.

Yuste, R. and Denk, W. (1995) 'Dendritic spines as basic functional units of neuronal integration', *Nature*, pp. 682–684. doi: 10.1038/375682a0.

Zemelman, B. V. *et al.* (2002) 'Selective photostimulation of genetically chARGed neurons', *Neuron*, 33(1). doi: 10.1016/S0896-6273(01)00574-8.

Zhang, F. *et al.* (2006) 'Channelrhodopsin-2 and optical control of excitable cells', *Nature Methods*, 3(10). doi: 10.1038/nmeth936.

Zhang, X. and Li, B. (2018) 'Population coding of valence in the basolateral amygdala', *Nature Communications*, 9(1). doi: 10.1038/s41467-018-07679-9.

Acknowledgments

I would like to express my gratitude to my PI, Andrea, for his invaluable guidance and his continuous support throughout my PhD journey. His expertise and constructive hints have been instrumental in advancing this research and fostering my personal and professional growth.

I am also deeply thankful to my thesis relators, Dr. Nelson Rebola and Dr. Naoya Takahashi, for their thoughtful feedback and constructive observations, which have helped refine this work and improve its scientific impact.

I would also like to thank my colleagues for their collaboration, discussions, and encouragement throughout this journey. Their support has made this experience not only productive but also enjoyable. I owe a special thanks to Dario Cupolillo—without him, this thesis wouldn't be what it is, or perhaps it wouldn't exist at all.

I would like to thank my family, who have always supported me and believed in my abilities. Their unwavering confidence in me has been a constant source of motivation and strength.

Lastly, I would like to thank the person who truly shared this experience with me, Alessandra, with the hope that this will be just one of many journey we'll share in life.